Epigenome priming dictates transcription response and white matter fate upon perinatal inflammation

Anne-Laure SCHANG[1,2,3*], Juliette van STEENWINCKEL[2,3†], Julia LIPECKI[6,†], Charlotte RICH-GRIFFIN[6], Kate WOOLLEY-ALLEN[6], Nigel DYER[5], Tifenn Le CHARPENTIER[2,3], Patrick SCHÄFER[6], Bobbi FLEISS[2.3,4**], Sascha OTT[7,‡,§], Délara SABÉRAN-DJONEIDI[1,2,‡,§], Valérie MEZGER[1,2,‡,§,$], Pierre GRESSENS[2,3,4,‡,§]

[1] Université de Paris, Epigenetics and Cell Fate, CNRS, F-75013 Paris, France
[2] Fédération Hospitalo-Universitaire FHU I2-D2, F-75019 Paris, France
[3] Université de Paris, NeuroDiderot, Inserm, F-75019 Paris, France
[4] Centre for the Developing Brain, Department of Division of Imaging Sciences and Biomedical Engineering, King's College London, King's Health Partners, St. Thomas' Hospital, London, SE1 7EH, United Kingdom.
[5] Department of Computer Science, University of Warwick, Coventry, CV4 7AL, United Kingdom
[6] School of Life Sciences, University of Warwick, Coventry, CV4 7AL, United Kingdom
[7] Warwick Medical School, University of Warwick, Coventry, CV4 7AL, United Kingdom

[$] Lead contact: valerie.mezger@u-paris.fr
[†]Equal contribution to the work
[‡] Equal contribution to the direction of the work
[§] Co-corresponding authors: : s.ott@warwick.ac.uk; delara.saberan@u-paris.fr; valerie.mezger@u-paris.fr; pierre.gressens@inserm.fr

[*] Present address: INSERM, UMR1153, Epidemiology and Biostatistics Sorbonne Paris Cité Center (CRESS), HERA team. Université de Paris, Faculté de Santé, Faculté de Pharmacie de Paris - 4 avenue de l'Observatoire – 75006 PARIS, France
[**] Present address: School of Health and Biomedical Sciences, RMIT University, Bundoora, VIC, Australia

ORCID numbers: AL Schang, 0000-0003-1712-8505; J van Steenwinckel, 0000-0003-3463-4856; N Dyer 0000-0001-6158-0510; P Schäfer 0000-0002-0366-6858; B Fleiss, 0000-0001-7828-673X; D Sabéran-Djoneidi, 0000-0002-2757-6419; V Mezger, 0000-0003-1623-6213; P Gressens, 0000-0002-0909-4221;

BIOLOGICAL SCIENCES: Neuroscience; Systems Biology; Developmental Biology

FUNDING Information
VM was funded by CNRS, Université Paris Diderot, Agence Nationale de la Recherche (« HSF-EPISAME », SAMENTA ANR-13-SAMA-0008-01) and FRA 2015/16. DSD was funded by Paris Diderot University for travel grant for SO. ALS was supported by a postdoctoral fellowship by SAMENTA ANR-13-SAMA-0008-01. PG was funded by Inserm, Université Paris Diderot, ANR-13-SAMA-0008-01, Fondation Grace de Monaco, PremUP, Fondation des Gueules Cassées, ARSEP, and an additional grant from "Investissement d'Avenir -ANR-11-INBS-0011-" NeurATRIS. BF acknowledges support from Cerebral Palsy Alliance, Australia. PG and BF acknowledge financial support from the Department of Health *via* the National Institute for Health Research (NIHR) comprehensive Biomedical Research Centre award to Guy's & St Thomas' NHS Foundation Trust in partnership with King's College London and King's College Hospital NHS Foundation Trust. JL, CR, and KWA were funded by the Biotechnology and Biological Sciences Research Council (UK) through the Midlands Integrative Biology Training Partnership (MIBTP). The supporting bodies played no role in any aspect of study design, analysis, interpretation or decision to publish this data.

Author's contributions

ALS performed bioinformatics microarray and ATAC-seq dataset analyses, as well as wet experiments, including the MACS-isolation of O4+ OPCs and RT-qPCR experiments, in association with JvS (experimental design, mouse treatment and cell sorting) and TLC (cell culture, cytokine quantification by luminex). BF contributed to the design of the project, and brought very helpful suggestions along the experimental process and writing of manuscript.

SO, DSD, PG and VM codirected the work. SO supervised JL, CRG, KWA and ND in their input ATAC-seq analyses and developed bioinformatic tools for testing for enrichment of paired motifs of transcription binding sites, and also proposed and performed the bioinformatic comparison between the epigenomic landscapes of OPCs and inflamed HAECs. PS co-supervised JL and CRG. DSD played a major role in suggesting the use of ATAC-Seq, animated the collaboration with SO, and performed the MACs-isolation of OPCs and ATAC-Seq data experiments with ALS whom she co-supervised with VM and PG.

PG scientifically co-directed with VM the project. In particular, he and BF were at the origin of the MACS-isolation of the OPCs and produced OPC transcriptomic datasets and initiated their analyses.

VM drove the study by proposing to analyze and intersect epigenomic data and transcriptomic data, for which she supervised DSD and co-supervised ALS; she wrote the paper with input from ALS, BF, SO, DSD, and PG.

Declaration of interests

The authors declare no competing interests.

Running title

Neuroinflammation uses primed epigenome

Summary

Inflammatory insults accompanying prematurity provokes diffuse white matter injury (DWMI) which is associated with increased risk of neurodevelopmental disorders: pre-term infants have a 10 to 18-fold increased risk of developing autism spectrum disorders, compared to term infants. DWMI is due to maturation arrest in oligodendrocyte precursor cells (OPCs). Using integrated genome-wide approaches in a validated mouse perinatal model of DWMI, induced by systemic- and neuro-inflammation based on repeated interleukin-1B administrations, we show that neuroinflammation induces limited epigenomic disturbances in OPCs. In contrast, we unravel marked transcriptomic alterations of genes of the immune/inflammatory pathways, which are expressed in unstressed OPCs and physiologically downregulated along OPC maturation. Consistently, we observe that transcription factors of the inflammatory pathways occupy DNA both in unstressed and inflamed OPCs. Thus, rather than altering genome-wide chromatin accessibility, neuroinflammation takes advantage of open chromatin regions and deeply counteracts the stage-dependent downregulation of these active transcriptional programs. Therefore, our study opens new avenues for the future development of targeted approaches to protect preterm brains.

Keywords: neuroinflammation; epigenome; transcriptome; oligodendrocyte precursor cell; immune/inflammatory pathway; perinatal model of white matter injury; prematurity

Highlights

- Limited epigenomic impact of inflammation on OPC maturation blockade
- Major transcriptomic disturbances take advantage of a primed epigenetic landscape
- Proinflammatory genes are active in OPCs and downregulated upon maturation
- Neuroinflammation counteracts both this downregulation and maturation in OPCs

INTRODUCTION

Premature birth, namely birth before 37 of 40 completed weeks, occurs in 8-13 % of all births worldwide and is the commonest cause of death and disability in children under 5 years of age (Delobel-Ayoub et al., 2009). Life-long morbidity is predominantly due to neurological damage, which altogether includes an array of effects, collectively called "encephalopathy of prematurity" (Volpe, 2009). Almost 10% of infants born before 33 weeks develop cerebral palsy and approximately 35% have persistent cognitive and neuropsychiatric deficits, including autism spectrum disorders and attention deficit/hyperactivity disorder (Bokobza et al., 2019). Although the most severe problems stem from extreme prematurity, even slight reductions in gestational length have significant adverse effects. One of the hallmarks of encephalopathy of prematurity is diffuse white matter injury (DWMI), which is considered a key target for neuroprotection and the prevention of long-lasting handicap. DWMI is due to oligodendrocyte maturation arrest, leading to hypomyelination and ultimately to defects in grey matter connectivity (Delobel-Ayoub et al., 2009; Ball et al., 2012; Billiards et al., 2008). In that context, neuroinflammation is a leading cause of encephalopathy of prematurity, serving as a central mediator of oligodendrocyte maturation defects and hypomyelination (Leviton and Gressens, 2007; Hagberg et al., 2015).

We have previously validated a mouse model of encephalopathy of prematurity that recapitulates arrest in oligodendrocyte maturation, hypomyelination, cognitive deficits and neuroinflammation, as seen clinically (Favrais et al., 2011; Krishnan et al., 2017; Shiow et al., 2017; Rangon et al., 2018). In this model, the common exposure of preterm-born infants to systemic and central inflammation (neuroinflammation) that is known to drive encephalopathy is mimicked by intraperitoneal (i.p.) administration of interleukin 1B (IL1B) from postnatal days 1 to 5 (P1-P5). Because in clinical conditions and diverse models of DWMI, males are more severely affected than females (Hagberg et al., 2015), the studies on oligodendrocyte precursor cells (OPCs) - and the present study - are performed in male animals. The developmental window (P1-P5) is equivalent to the high-risk window for encephalopathy of prematurity in infants, [23-32]-week gestational age. This paradigm of DWMI causes long-term myelination defects (Favrais et al., 2011), but the delicately choreographed programs that control OPC maturation, which are disturbed in this model - creating a cell fate issue - are not understood and remain to be enlightened.

Here, using a purified population of premyelinating OPCs, from this animal model, we have explored, through integrated genome-wide approaches, the contribution of epigenomic and transcriptomic disturbances to the OPC dysmaturation. We show that at P5 a limited number of chromatin regions are perturbed. We also find that the genes, whose expression levels are the most significantly altered by neuroinflammation, are involved in the immune system and inflammatory response. These genes, which include cytokines and chemokines, are unexpectedly also expressed by OPCs in normal conditions, in a developmentally regulated manner: their expression is higher at early stages and downregulated over the course of their maturation. The stage-dependent downregulation of these genes is perturbed in OPCs isolated from our inflammatory model of encephalopathy, which provokes a marked upregulation of their expression – likely participating to the failure of these cells to mature correctly.

These major transcriptomic disturbances surprisingly occur in genes which exhibit no overt changes in chromatin accessibility at P5. Indeed, our evidence suggests that neuroinflammation takes advantage of transcriptional programs that are active at the time of exposure – namely open chromatin regions - and disturbs their developmental regulation.

We have therefore unraveled a mechanism by which neuroinflammation acts on OPCs and could participate in maturation arrest in a model mimicking perinatal inflammation in preterm born infant. Indeed, the unexpected expression of numerous inflammatory genes by OPCs during their normal stage-dependent maturation likely paves the way for intricate interference between the response to neuroinflammatory insults and the white matter developmental program, with important implications for therapeutic strategies.

143 **RESULTS**

144 **Purity and quality of the O4+-purified cell populations used for exploration of the epigenome and transcriptome**

145 In our previous studies, we have demonstrated that oligodendrocyte maturation arrest is a hallmark of the
146 neuropathy caused by neuroinflammation that is triggered by intraperitoneal IL1B administration (IP). As outlined
147 above and in Figure 1, IL1B was administered between P1 and P5 (versus PBS as a control; Figure 1; (Favrais et al.,
148 2011; Krishnan et al., 2017; Shiow et al., 2017; Rangon et al., 2018); this period mimics chronic exposure to systemic
149 neuroinflammatory mediators from 23-32 weeks of gestation in the infant. Using magnetic-activated cell sorting
150 (MACS), we isolated at P5 the premyelinating OPC population (O4+ OPCs) from male cortices in each condition
151 (Figure 1). O4 is considered a pan-marker of late OPCs in humans and mice (Volpe, 2009; Favrais et al., 2011). We
152 evaluated the purity of the O4+ cell population by a panel of diverse approaches at each step during the course of
153 our study (Figure S1). Notably, O4+ OPC cells were directly isolated from the pup cortices, and immediately and
154 directly processed without culturing. By performing RT-qPCR analyses, we demonstrated that this population,
155 expressed *Myelin binding protein* (*Mbp*) mRNAs, a marker of myelinating oligodendrocytes, whose transcription
156 starts in pre-myelinating oligodendrocytes, contrary to microglial (CD11B+) MACS-isolated fractions (Figure S1A).
157 Conversely, we found that the levels of the microglia marker mRNAs, CD11B (*Itgam*, *Integrin alpha M* gene) were
158 almost undetectable in this O4+ cell population. This population therefore corresponds to premyelinating OPCs. In
159 independent RT-qPCR experiments, as expected based on previous studies using this model (Favrais et al., 2011),
160 we observed that the expression of *Id2*, encoding a transcriptional inhibitor of oligodendrocyte differentiation, was
161 increased in O4+ OPCs in response to neuroinflammation, whereas that of myelination-associated genes was
162 slightly, but reproducibly, reduced (Figure S2A).

163 Overall, these data show that the cell population isolated by our MACS-protocol is predominantly enriched
164 with O4+ OPCs and exhibits, as expected, hallmarks of maturation arrest in response to neuroinflammation induced
165 by intraperitoneal administration of IL1B.

166

167 **The epigenome of OPCs is globally preserved in response to systemic IL1B exposure**

168 We first investigated the impact of neuroinflammation the integrity of the chromatin landscape in OPCs using
169 ATAC-Seq (Buenrostro et al., 2013; *Assay for Transposase-Accessible Chromatin with high-throughput sequencing*;
170 Figure 1). Using the bioinformatics workflow described in Figure S2B (see Material and Methods) including the
171 MACS2 (Zhang et al., 2008) and EdgeR (Robinson et al., 2010) software tools, we obtained an average of 72 million
172 Tn5 transposase-integrated mapped reads per sample, representing a total of 213,246 statistically significant peaks
173 (MACS2; FDR < 0.05; Table S1 and S2; Dataset S1). Analysis of the insert size distributions showed the expected
174 nucleosome-induced pattern and 10.4bp periodicity with good consistency across samples, an indication of high
175 data quality (Figure S2C; Buenrostro et al., 2015).

176 The number of reads, which reflects chromatin accessibility, was determined for each sample in the 213,246
177 peaks. We performed principal component analysis (PCA) on our samples and observed that principal component
178 1 (PC1) accounted for 42% of the variance and separated samples from control and neuroinflammation-exposed
179 OPCs (Figure 2A). We obtained similar results using the EdgeR MDS function (Figure S3A). This shows that a large
180 proportion of the variance in this dataset can be explained by the exposure to neuroinflammation. Among the
181 213,246 significant peaks, only 524 regions were open or closed in response to IL1B (FDR < 0.05, Figure 2B; Figure
182 S3B; Table S3). The majority of peaks with differential chromatin accessibility was more open in IL1B, compared to
183 PBS conditions (Figure 2B,C). The extent of changes in chromatin accessibility was small, with fold-changes of most
184 peaks only mildly deviating from sample-to-sample variability (Figure 2B). The median fold-change of differentially
185 open regions was 2.03-fold.

186 We next annotated the 213,246 peaks using HOMER annotatePeaks function (Heinz et al., 2010). Peaks were
187 mostly distributed in intergenic and intronic regions and were enriched in gene regulatory regions and gene bodies
188 (Figure S3C). A similar distribution was observed for the 524 differential peaks (Figure S3C). Representative peaks
189 showing increased, reduced, or unchanged chromatin accessibility are illustrated in Figure 2D-F. We assigned
190 differential peaks to genes, likely affected by chromatin alteration, based on proximity to their transcription start
191 site (TSS), and we performed gene ontology (GO) analyses, using David6.8 (Huang et al., 2009a; Huang et al., 2009b)

192 for the 485 corresponding genes, of which 344 were assigned a GO-term. The top ten GO-terms ranked according
193 to their FDR, belong to pathways relevant for neural development (regulation of cell migration, cell adhesion, and
194 neuron projection development), but none of them showed FDR < 0.05 (Figure S3D; Table S4).
195 Our results thus reveal that only 0.25% of open chromatin regions show differential chromatin accessibility
196 in P5 OPCs that are isolated from a model of inflammation-driven encephalopathy, showing that the chromatin
197 landscape is globally preserved, in terms of accessibility,

198 **Major transcriptomic impact of neuroinflammation on the immune/inflammatory pathway in O4+ OPCs**

199 We analyzed gene expression in isolated O4+ OPCs using microarray analysis. We compared six independent
200 samples of O4+ OPCs from IL1B-exposed mice to six independent samples from PBS-treated (control) mice. Induced-
201 neuroinflammation mainly triggered upregulation of gene expression: 1,266 genes were up-regulated and 454
202 downregulated, which corresponded to 1,872 and 699 probes, respectively (FC +/-1.5; FDR < 0.05; Figure 3A; Table
203 S5). As expected based on previous work in this model (Favrais et al., 2011) and from our validation experiments by
204 RT-qPCR for O4+ OPC isolation (Figure S2A), the analysis of our microarray data revealed that the expression of
205 genes associated with myelination (*Mbp*, *Mog*, *Mag*, *CNPase*, *Plp1*; which are still lowly expressed at P5 in normal
206 conditions) were downregulated by neuroinflammation, whereas that of *Id2* was upregulated (Favrais et al., 2011);
207 Figure S4A). These results likely reflected OPC maturation blockade (Favrais et al., 2011). Strikingly our GO analysis
208 of these upregulated genes pinpointed the immune system and inflammatory response in the top 5 most
209 statistically significant pathways (DAVID 6.8; Figure 3B; Table S6). The analysis of downregulated genes indicated
210 that these belonged to pathways linked to development, but with lower statistical relevance (Figure S4B).
211 Interestingly, the vast majority of the genes belonging to the immune system and inflammatory response pathways
212 and whose expression was significantly altered, appeared to be upregulated (220/262); Figure 3C). Using RT-qPCR
213 on independent samples, we confirmed the induction of the expression of known players of these pathways:
214 cytokines, chemokines, interleukins and their receptors (Figure 3D).
215

216 **OPCs intrinsically produce cytokine and chemokines in response to IL1B**

217 We confirmed that cytokine and chemokine genes were upregulated by neuroinflammation in O4+ OPCs
218 *per se*, and excluded the possibility that the upregulation of immune and inflammatory genes was due to
219 contamination of O4+ OPCs with microglia, using different approaches. In this model of neuroinflammation, we
220 have previously published microarray analyses of the transcriptomic profiles in microglia (CD11B+ MACS-isolated
221 MG cells; (Krishnan et al., 2017; Van Steenwinckel et al., 2019). These CD11B+ cells were obtained from the same
222 animals as the O4+ OPC populations from this study, by sequential MACS-based isolation of O4+ OPCs and CD11B+
223 microglia cells. We compared the microarray gene expression profiles in the previously assessed CD11B+ cells to
224 the list of 262 genes found in OPCs and corresponding to inflammation and immune pathways (Figure 4A; Figure
225 S1B; dataset from (Krishnan et al., 2017). O4+ OPCs and CD11B+ MG populations exhibited remarkable differences
226 in gene expression profiles in response to neuroinflammation, both in the magnitude and direction of expression
227 changes (Figure 4A; Figure S1B). Notably, the upregulation of these genes in microglia was greatest at P1 and their
228 expression at P5 has already recovered, reaching basal levels comparable to that of PBS samples, while in OPCs
229 their expression remained elevated (Krishnan et al., 2017; Figure 4B). Those data were confirmed by RT-qPCR in
230 independent O4+ OPC and CD11B+ MG samples, and extended to astrocytes (GLAST+ MACS isolation; Figure 4B).
231 Specifically, neither CD11B+ MG, nor GLAST+ astrocytes showed any increase in the expression of selected cytokines
232 and chemokines at P5, in contrast to O4+ OPCs (illustrated here for *Ccl2*, *Cxcl1* and *Cxcl10*; Figure 4B). Altogether,
233 these results indicate that the upregulation of immune and inflammatory pathway in O4+ OPCs in response to
234 neuroinflammation in our microarray analyses at P5 cannot be attributed to contamination of OPCs by microglia,
235 nor astrocytes.
236 In addition, we also ruled out the possibility that a very low number of contaminating MG would be
237 responsible for producing cytokine and chemokine transcripts, by investigating the chromatin accessibility of genes
238 specific for OPCs or MG in ATAC-Seq analyses. We showed that *Olig2*, a pan-oligodendrocyte marker, which is not
239 expressed by MG, displayed open chromatin structure in our O4+ OPC population, as indicated by the presence of

ATAC-Seq peaks, but showed closed chromatin conformation in purified MG (data mining from Matcovitch-Natan et al. 2016; Figure S1C,D). Conversely, as expected, the MG-specific gene, *Itgam*, exhibited closed chromatin conformation in O4+ OPCs, in contrast to what was observed in MG (Figure S1C). So, if the cytokine and chemokine transcripts were produced by contaminant MG and not by OPCs, we should have seen a stronger ATAC-seq peak in MG than in OPCs at corresponding genes. This is not what we observed. When investigating the chromatin status of cytokine and chemokine genes in our MACS O4+ OPC population, we detected ATAC-Seq peaks with two different profiles as illustrated in Figure S1D: i) *Cxcl1*, that was found in an open chromatin state in the MACS-isolated O4+ OPCs population, but not in isolated MG. This indicates that this gene is in an open chromatin conformation in OPCs, whereas it is not in MG. This therefore implies that MG cannot be the major contributor to the synthesis of these molecules in the MACS-isolated O4+ OPC population; ii) *Ccl2* or *Cxcl10* were found in an open conformation in MACS-isolated O4+ OPCs, as well as in isolated MG, but, since *Itgam* was not detected as open in the MACS-isolated O4+ OPC population, it means that these peaks mainly correspond to the *Ccl2* or *Cxcl10* gene status that exists within MACS-isolated O4+ OPCs, and not within MG (Figure S1D; note that the peak profiles of *Cxcl1, Ccl2* or *Cxcl10* are also illustrated in Figure 2F, but, in that case, separately showing PBS1-3 and IL1B 1-3 samples).

We concluded that contamination of MACS-isolated O4+ OPCs by MG, if any, is only very minor in this study, as it is undetectable in our ATAC-Seq experiments. Such contamination therefore cannot account for the open chromatin status detected in cytokine or chemokine genes in the MACS-isolated O4+ OPC population.

To further verify the potential for production of inflammatory players by OPCs in response to inflammation, we isolated primary OPCs, grew them *in vitro* and treated these cultures with IL1B (Figure 4C). We detected significant induction of the production of seven cytokine and chemokine proteins *via* Luminex in the supernatant of IL1B-treated MACS-isolated primary O4+ OPCs, cultured for 24 or 72 hours (Figure 4D). We also confirmed the upregulation of these inflammatory and immune mediators at mRNA levels (Figure S4C).

In conclusion, these data strongly support the hypothesis that, at P5, O4+ OPCs are able to intrinsically synthesize inflammatory and immune pathway proteins in response to exposure to inflammatory stimuli.

Major involvement of transcription factors of the immune and inflammatory pathways in O4+ OPCs

To globally examine the contribution of modifications of chromatin accessibility to the transcriptomic changes, we intersected our ATAC-Seq data (213,246 peaks, corresponding to 20,108 gene names) and our microarray data (limited to 25,294 genes with annotated ID). We found 16,883 genes in common between the two datasets, of which 1,333 genes showed altered expression after IL1B exposure and 404 peaks showed differential chromatin accessibility. By performing the intersection of the 1,333 differentially expressed genes with genes located nearby the differential 404 ATAC-Seq peaks, we identified 53 genes representing a statistically significant overlap between transcriptomic and epigenomic changes. (Figure 5A; $p= 1.7\ e^{-4}$; hypergeometric test; Table S7).

In order to maximize the chance of attributing peaks to relevant genes, we reasoned that peaks corresponding to opening or closing of the chromatin and lying within +/- 8kb around a TSS were most likely to contribute to the regulation of the expression of the corresponding gene. Taking this into account, we identified 15 genes showing differential expression and exhibiting modifications of the chromatin landscape in their vicinity, which corresponded to 20 % of the ATAC-Seq peaks present in +/- 8 kb around the TSS (Figure 5B; $p= 8.74\ e^{-5}$; Table S8). Among these 15 genes, 10 were involved in the immune system and inflammatory response pathways: *Cd14, Cwc22* (Figure 2E), *Hmha1, Ifit3, March1, Nckap1l, Slfn2, Slc15a3, Tlr1, Tnfsf14, Tnfrsf12a* (Table S8). Interestingly, *Hif3a*, a gene recently identified in models of inflammation, was also included in this list (see discussion; Figure 2D).

In summary, the immune system and inflammatory response pathways were prominently represented in the lists of genes showing marked dysregulation of their expression upon exposure to neuroinflammation, and associated to two different chromatin behaviors: 1) a limited number of genes showed differential chromatin accessibility upon IL1B exposure (Figure 5A,B); 2) the majority of the genes annotated in the top 5 most enriched GO-terms displayed no major changes in chromatin accessibility. Indeed, in this case, the chromatin was already in an open conformation in the PBS samples (examples shown in Figure 2F).

289 **Identification of combinatorial transcription factor binding in immune system and inflammatory pathways**

290 In the large majority of instances where neuroinflammation altered gene expression, we observed that
291 the chromatin was already open and remained unchanged in response to neuroinflammation (examples shown in
292 Figure 2F). As such, we investigated the putative involvement of transcriptional regulators as primary mediators of
293 alteration in gene expression. We searched for enrichment in transcription factor (TF) binding sites (TFBS) using
294 HOMER and known motifs in the ATAC-Seq peaks adjacent to differentially regulated genes (up and downregulated
295 genes, termed "ALL"). We chose to focus on ATAC-Seq peaks within a distance of +/- 8 kb relative to the TSS of these
296 genes. Motifs for members of the IRF (interferon-regulatory factor) family appeared at the top of the list with the
297 strongest scoring results (Figure S5A). A list of similar motifs, including motifs for the NFκB family members, was
298 found with comparable scoring results, as well as p-values, in the peaks adjacent to upregulated genes (termed
299 "UP"; Figure S5B). Notably, the composite site PU.1-IRF8 and were enriched in "UP" genes (Figure S5B).

300 Because we suspected that these TFs might work together (Yanai et al., 2012), we investigated the
301 occurrence of paired motifs in the peaks located in +/- 8kb regions around the TSS of differentially regulated genes,
302 as described in Materials and Methods. The analysis of peaks corresponding to downregulated genes did not reveal
303 any paired motif enrichment, compared to random occurrence in all peaks. In contrast, the analyses of ATAC-Seq
304 peaks associated with upregulated genes revealed the existence of paired TFBS motifs, with marked involvement
305 of TFBS from the IRF family, PU.1/SPI1, *Isre* (Interferon-Stimulated Response Element), NFκB, and AP-1 family
306 (Figure 5C; Table S9).

307 To investigate whether the occurrence of these motifs corresponded to the binding of TFs, we tested the
308 motif occupancy on DNA in PBS and IL1B conditions. For this, we used the Wellington algorithm (Piper et al., 2013),
309 which is highly accurate in inferring protein (TF)-DNA interactions. We investigated the presence of footprints
310 corresponding to occupied TFBS and their motif content, located within significant ATAC-Seq peaks, adjacent to
311 differentially regulated genes. The average footprint profiles, produced for the top 6, high-ranked, HOMER motifs
312 (Figure S5A,B) are illustrated for IRF1, IRF2, IRSE and NFκB in Figure 5D (using data from both conditions, PBS plus
313 IL1B) and in Figure S6A (PBS, upper panels; IL1B, lower panels). The dip in the number of reads at the center of the
314 sharp average profile (indicated by brackets) was strongly suggestive of effective TF binding (Figure 5D and S6A). In
315 contrast, PU.1-IRF8 and PGR (Progesterone Receptor) average footprint exhibited sharp internal spikes, suggestive
316 of transposase insertion bias (Green et al., 2012, Figure S6B). Interestingly, there was little difference in the average
317 footprint profiles for all these TFs, when considering either PBS samples only or IL1B samples only, indicating that
318 these TFs (or TFs binding similar motifs), might already bind DNA at the corresponding motifs in unstressed,
319 physiological conditions (Figure S6A).

320 Altogether, these results indicate that key TFs involved in the immunity and inflammatory processes are
321 bound in a significant number of open regions located in the vicinity of genes that are differentially upregulated by
322 neuroinflammation. The binding of such TFs is coherent with the prominent upregulation of proinflammatory
323 cytokine and chemokine genes, and other genes of the immune system and inflammatory pathways. In addition,
324 because footprint profiles were similar in PBS and IL1B conditions, our data suggest that, at P5, these TFs might be
325 positioned in these regions before exposure to neuroinflammation.

326 There was no evidence for footprints in peaks adjacent to downregulated genes (data not shown).
327 Moreover, the search for de *novo* motifs in ATAC-Seq peaks near differentially expressed genes did not reveal
328 statistically relevant motif associated with *bona fide* average footprints (data not shown).

329

330 **Constitutive expression of genes of the immune and inflammatory pathways at early stages of OPC maturation**
331 **trajectory, in unstressed conditions**

332 At this step of the study, we had shown that P5 isolated O4+ OPCs were able to induce the expression of
333 genes belonging to the immune system and inflammatory response pathways, in response to neuroinflammatory
334 challenge. We had also shown that these major alterations in gene expression occurred without major modifications
335 in chromatin accessibility, but that key TFs controlling these pathways were bound to these open regions both in
336 the control (PBS) and neuroinflammatory (IL1B) conditions. These observations suggest that the epigenomic profiles
337 associated with neuroinflammation-induced genes exhibit "neuroinflammatory-like" patterns, prior to IL1B

338 injections (*i.e.* open chromatin conformation). Therefore, we wondered if the transcription of these genes may
339 already be activated at a physiological level in OPCs during normal development and further upregulated by
340 exposure to neuroinflammation.

341 To assess this hypothesis, we MACS-isolated O4+ OPCs at P3, P5, and P10 from our model of preterm
342 neuroinflammatory injury, and indeed, we detected, by RT-qPCR, the presence of cytokine and chemokine mRNA
343 in O4+ OPCs in control conditions (Figure 6A). These mRNA levels were greatest at P3 and significantly decreased in
344 a stage-dependent manner, between P3 and P10 (Figure 6A). In addition, we verified that our control condition (i.p.
345 PBS) did not constitute a stress, *per se*, that would induce the expression of cytokine and chemokine genes.
346 Comparing MACS-isolated O4+ OPCs from naïve (untreated) and PBS-treated pups at P5, we observed similar levels
347 of cytokine and chemokine gene expression, in RT-qPCR experiments (Figure S7B). This shows that PBS injection is
348 not responsible for constitutive cytokine and chemokine mRNA levels at P5. In contrast, OPCs isolated from IL1B-
349 treated mice exhibited elevated levels of cytokine and chemokine mRNAs compared to naïve or PBS OPC samples,
350 as expected (Figure S7B). Moreover, we confirmed that the constitutive expression of cytokine and chemokine
351 genes also occurred in normal conditions in the murine oligodendroglial cell line, Oli-neu (Figure 6B,C), therefore
352 indicating that the detection of such mRNAs is neither due to contamination of O4+ OPCs by MG, nor to their
353 isolation mode, nor to the intraperitoneal injection *per se*. We also showed that this constitutive expression
354 decreased during Oli-neu differentiation – using two protocols – as it was observed during the O4+ OPCs maturation
355 trajectory (Figure 6C and Figure S1E). These data demonstrated that O4+ OPCs intrinsically transcribe cytokine and
356 chemokine genes at an early OPC stage (P3), and that the expression of these genes is gradually downregulated
357 during their maturation process between P3 and P10, in a physiological and developmental manner. This
358 constitutive transcription is in line with the small extent of chromatin accessibility changes of these genes that we
359 observe at P5 (Figure 2F).

360 To further confirm our assumption that, in OPCs, at P5, the chromatin of neuroinflammation-induced genes
361 exhibited "neuroinflammatory-like" signatures, prior to IL1B-treatment, we formulated and performed an
362 additional analysis, taking advantage of an existing public ATAC-seq dataset from a similar control versus treatment
363 study, which used IL1B stimulus on human adult aortic endothelial cells (HAECs) isolated from aortic trimmings of
364 donor hearts (Hogan et al., 2017; "HAEC dataset"; NCBI Gene Expression Omnibus; accession no: GSE89970).
365 Through a cross-species comparison, our aim was to explore global chromatin landscape similarities (or lack thereof)
366 between both control and IL1B-treated, in adult (HAEC) versus neonates (O4+ OPC) samples. First, both datasets
367 were limited to chromatin regions annotated with matching 1-to-1 gene orthologs and located within ±2 kb of a TSS
368 as described in Material and Methods. In total, we were able to match 7,739 peaks between the two datasets,
369 including 100 regions, which were found to be different between the control and IL1B conditions, in the HAEC
370 dataset. Subsequent cross-comparison of these regions reported no significant difference between both O4+ OPC
371 samples and the HAEC IL1B-treated sample. In contrast, both O4+ OPC samples showed significant differences (p-
372 value < 10^{-15}) to the HAEC control sample (Figure S7C,D; Table S10). These findings reveal a characteristic
373 "neuroinflammatory-like" pattern in the chromatin profiles of OPCs isolated from both inflammation-exposed and
374 control mice, which is indicative of an inflammation-like signature that is already present at basal level in developing
375 OPCs. The results thereby reinforce our findings about cytokine and chemokine gene expression in unstressed and
376 stressed O4+ OPCs.
377

378 **Correlative upregulation of genes of the immune/inflammatory pathway and downregulation of the myelination**
379 **program in an oligodendroglial cell line upon inflammatory stimulus.**

380 Our results suggest that 1) there is a specific and restricted time-window for the endogenous expression of
381 the cytokine and chemokine genes along the OPC maturation trajectory; 2) that, in response to *in vivo* IL1B-induced
382 neuroinflammation, which is known to result in a blockade of OPC maturation (Favrais et al., 2011), the
383 overexpression of the genes of the immune/inflammatory pathway strikingly correlates with the reduction of the
384 expression of the myelination programme *in vivo* (Figure 6A; Figure S7A). This is recapitulated in an oligodendroglial
385 cell line *in vitro* (Figure 6B,C and Figure S1E). To further explore the link between these two processes, we
386 investigated the response of the Oli-neu cell line to an inflammatory stimulus during its differentiation time-course.

We showed that *ex vivo* treatment of the Oli-neu cell line by TFN-alpha compromised the expression of genes of the myelination programme - as expected -, which is a hallmark of differentiation blockade (illustrated by *Cnp*, *Mbp* gene expression; Figure 7). In addition, it also induced concomitant strong and abnormal overexpression of genes of the immune/inflammatory pathway, thereby counteracting the physiological decrease of cytokine/chemokine expression normally observed during differentiation (Figure 7; here, illustrated for *Ccl2 and Cxcl10*). These data indicate that exacerbating the immune/inflammatory phenotype would participate to differentiation blockade.

394 **DISCUSSION**

395 The main goal of our study is to decipher molecular mechanisms that are triggered by neuroinflammation
396 in a context leading to OPC maturation arrest and white matter injury. Most of the studies on prenatal stress has
397 focused on the disturbances of epigenetic marks and has not really addressed the robustness versus vulnerability
398 of the epigenome, towards these insults (Schang et al., 2018). Moreover, they were performed on the whole brain
399 or dissected regions. There are therefore two main interests in our study.

400 The first major interest of our study is to use a purified population of OPCs, based on the O4 marker to
401 investigate the respective epigenomic and transcriptomic contributions to the disturbances induced by
402 neuroinflammation. To do so, we carefully assessed the purity of our isolated populations by different means and
403 at each step of our study, as summarized in Figure S1. Globally, we showed that specific markers of MG (and
404 astrocytes; Figure 4) are unexpressed in the isolated O4+ OPC population, based on transcriptomic and RT-qPCR
405 data. Moreover, the chromatin conformation of the corresponding MG-specific genes is inaccessible, based on
406 ATAC-Seq data, in contrast to that of chromatin regions of genes characteristic of OPCs. These data indicate that
407 our O4+ population is highly enriched in OPCs. Moreover, we could recapitulate in an oligodendroglial cell line the
408 two major aspects of normal and perturbed OPC maturation that we unraveled in O4+ OPCs: 1) the constitutive
409 expression of cytokine and chemokine genes in unstressed conditions and its physiological downregulation during
410 differentiation; 2) the upregulation of these genes in response to inflammatory insult. In addition, these genes
411 encoding cytokines and chemokines are in a closed chromatin conformation in MG, whereas they are in an open
412 conformation in both unstressed and stressed OPCs. Therefore, the assessment of the purity and functionality of
413 this isolated O4+ OPC population is built on a corpus of arguments that altogether lead to the conclusion that O4+
414 OPCs are able to constitutively synthesize molecules belonging to the immune/inflammatory pathways.

415 The second interest of our study is to show that, surprisingly, the epigenome of OPCs is globally preserved
416 in response to neuroinflammation, since only a very restricted number of regions undergo opening or closing of the
417 chromatin. Rather, our results indicate that neuroinflammation has a major impact at the transcriptomic level, by
418 disturbing the transcription of genes that are already active in OPCs at the time of exposure, under unstressed
419 conditions. Indeed, one route of entry for neuroinflammation is the remarkable capacities of premyelinating O4+
420 OPCs to produce immunomodulators. More precisely, the developmental control of their synthesis – namely,
421 expression at P3 and downregulation at P5 and P10 – is highjacked by neuroinflammation, which provokes abnormal
422 overexpression of these genes at a stage at which they should be downregulated. As such, this process occurs with
423 limited effects on chromatin accessibility. In other words, rather than remodeling the epigenetic landscape, the
424 response to neuroinflammation takes advantage of and place in a "primed" epigenetic landscape. Such a
425 mechanism is reminiscent of what happens in response to cellular stress, involving the heat shock pathway driven
426 by the Heat Shock transcription Factors, which is "pre-wired" by the chromatin architectural characteristics (HSFs;
427 Vihervaara et al., 2017; Vihervaara et al., 2018). Interestingly, a similar situation has been observed during learning
428 and memory processes, where increase in the levels of histone posttranslational modifications seem restricted to
429 genes that are already active in the naive state, while, conversely, global histone modifications are vastly uncoupled
430 from changes in gene expression (Halder et al., 2016).

431 In line with the expression of genes of the inflammatory pathway in OPCs both under unstressed and
432 stressed conditions, we found that, globally, characteristic binding sites for TFs involved in the
433 immune/inflammatory pathway are occupied before and after exposure to neuroinflammation. However, our
434 finding of existing paired binding motifs for these TFs, in ATAC-Seq peaks, suggest that these factors can act in a
435 combinatorial mode and that changes in their combination (and/or activity, as observed in other contexts; Mancino
436 et al., 2015) might account for the increase in the transcription of the corresponding genes that we detect upon
437 neuroinflammation exposure.

438 Our data also nurture an underlying and emerging concept: molecules, which have been historically
439 identified and studied as key mediators of stress responses and guardians of cell or organism homeostasis, are also
440 pivotal in physiological conditions for normal development (Cardona et al., 2008). Emblematic examples are
441 represented by TF families, like NFkB (Espín-Palazón and Traver, 2016), HSFs and their target genes encoding the
442 heat shock proteins (HSPs; Abane and Mezger, 2010; Chang et al., 2006; Gomez-Pastor et al., 2018), and by critical

443 players of the unfolded stress response (UPR; Laguesse et al., 2015). Whether these two apparently distinct
444 functions have emerged concomitantly in evolution or not is unclear, but for technical and practical reasons, the
445 roles of these molecules in normal development have been understudied. The stage-dependent production of
446 inflammatory players by prenatal OPCs during the time-course of their maturation, as well as their potential role in
447 brain formation, is therefore less unexpected than it appears. Accordingly, it has been extensively reported in the
448 literature that OPCs and mature oligodendrocytes of the adult brain can express key players of immune and
449 inflammatory pathways in pathological conditions. This includes studies of patients affected by multiple sclerosis
450 (MS) or in *in vivo* models of experimental autoimmune encephalomyelitis (EAE; reviewed in Zeis et al., 2016). Here,
451 we show that P5 O4+ OPCs express genes and proteins associated with inflammatory pathways in normal
452 conditions. As such, OPCs during normal development thus display properties similar to that ascribed to adult OPCs
453 and mature oligodendrocytes, which can shape the inflammatory environment, or - in the perspective brought by
454 the new concept mentioned above - could perform a trophic role on their environment at defined time-windows.
455 Our results are also in line with previous results showing that OPCs, derived *in vitro* from neurospheres, can activate
456 cytokine genes in an EAE model (Cahoy et al., 2008). In a more original manner, we also unravel the physiological,
457 constitutive expression of cytokine and chemokine genes in normal O4+ OPCs at an early postnatal stage. In line
458 with our findings, Zeis et al. (2016) revisited published microarray data sets (Cahoy et al., 2008) and pointed out the
459 expression of genes belonging to the GO:term "immune system process", in PDGFRa+ unstressed OPCs, which
460 reinforces our data.

461 Among the genes belonging to the immune system and inflammatory pathways and undergoing
462 dysregulated expression upon exposure to neuroinflammation, only a limited number exhibit significant chromatin
463 remodeling. Hypoxia-Inducible Factor 3, *Hif3a*, is one of them and was shown to be regulated, in an oxygen-
464 independent manner, in two distinct models of inflammation, in non-neural cells (Kumar et al., 2015; Cuomo et al.,
465 2018). Interestingly, in parallel of our data, Cuomo et al. (2018) established that proinflammatory cytokines are
466 responsible for the activation of *Hif3a* gene, through epigenetic changes and the involvement of NFκB.

467 One question is the functional impact of the opening or closing of the chromatin in response to
468 neuroinflammation, in regions that we have identified by ATAC-Seq, since most of them do not correlate with major
469 transcriptional changes. This raises three interpretations. Firstly, the transcriptomic impacts of these epigenomic
470 modifications might be "buffered", thanks to the binding of different sets of TFs, which would deserve further
471 investigations. Secondly, TFs, which are multifaceted drivers, remodel the chromatin state and genome topology,
472 often before changes in gene expression can be observed, as was demonstrated in studies on the molecular basis
473 of cell fate (Stadhouders et al., 2018). These modifications of the chromatin landscape could thus constitute an
474 Achilles' heel for transcriptomic disturbances, that would occur either at later maturation stages, at temporal
475 distance from the insult, or upon a second hit of neuroinflammation. The occurrence of additional inflammatory
476 insults is relevant because, besides exposure to prenatal inflammatory insults - which is mimicked by our model -,
477 preterm babies also face a heavy burden in terms of postnatal inflammatory insults, representing additional
478 neuroinflammatory hits (Barnett et al., 2018). Thirdly, one other exciting possibility is that, in the genome, these
479 TFs involved in immune and inflammatory pathways might also work at long-distance from their dysregulated target
480 genes, which would involve remodeling at multiple architectural levels (chromatin looping, sub-TADs (topologically
481 associated domains) connectivity etc.).

482 Finally, besides these considerations, the entry route for neuroinflammation is represented by the
483 constitutive and stage-dependent synthesis of cytokines and chemokines by premyelinating OPCs in normal
484 conditions, which empowers neuroinflammation to impact OPC maturation. This entry route can thus be envisioned
485 as recapitulating and intermingling both injurious and developmental aspects, as already expected from the field
486 (Volpe, 2011; Deverman and Patterson, 2009; Mancino et al., 2015). Indeed, by counteracting the tightly regulated
487 physiological expression of cytokines and chemokines by O4+ OPCs at P3, that is programmed to gradually decrease
488 in a developmental, stage-dependent manner (here shown between P3 and P10), the neuroinflammatory insult
489 might compromise the premyelinating OPC cell fate. Although the causality of the abnormal upregulation of
490 immune/inflammatory modulators by OPCs on their maturation is difficult to prove in our system, it is strongly
491 supported by an array of arguments: First, we can reproduce the correlation between the upregulation of cytokine

492 and chemokine gene expression and the downregulation of the myelin markers in an oligodendroglial cell line, upon
493 proinflammatory exposure to TNF-alpha. Second, Moyon et al. pointed out the role of IL1B and CCL2 production by
494 premyelinating OPCs in modulating their motility capacities and eventually differentiation (Moyon et al., 2015).
495 Third, CXCR2 counteracts adult OPC differentiation and myelination potential, in a model of multiple sclerosis, by
496 interfering with the PI3K/AKT/mTOR pathway, thereby strongly reinforcing the possibility of a role of cytokines and
497 chemokines in OPC maturation during development (Wang et al., 2020). One possible pathway for the
498 counteracting effects of cytokines and chemokines on OPC differentiation is that their production could regulate
499 the recruitment by OPCs of other cells that are known to influence OPC maturation (like microglia; (Jana and Pahan,
500 2005; Balabanov et al., 2007).

501 In conclusion, in the context of a chronic-perinatal systemic inflammation, the epigenome seems globally
502 preserved in premyelinating OPCs, in terms of chromatin accessibility, suggesting that the contribution to OPC
503 blockade is mostly driven by transcriptomic disturbances. These transcriptomic perturbations concern
504 transcriptional programs that are already active at the time of exposure, and, most prominently, those involved in
505 the immune system and inflammatory pathways. Our results have important therapeutic consequences: because
506 of the striking intertwining between the injurious and developmental facets of these inflammatory mediators, we
507 should reconsider that global targeting of this pathway might constitute a therapeutic option. One conclusion
508 emerging from our study is that the TFs involved in response to neuroinflammation in OPCs seem to be already at
509 play in normal OPCs to control the developmental transcription of these genes. In addition, some of them work in
510 combination as suggested by their pairing profiles. Our work thus paves the way of future studies that would allow
511 the design of a therapeutic strategy, based on subtle manipulation of the activity of TFs, using appropriate cocktails
512 of low-dose modulators.
513

514 **MATERIALS AND METHODS**

515 **Animal Model**

516 Experimental protocols were approved by the institutional review committee (under the following
517 reference by the French Ministère de l'Enseignement Supérieur et de la Recherche (#2016040414515579) and met
518 the guidelines for the United States Public Health Service's Policy on Humane Care and Use of Laboratory Animals
519 (NIH, Bethesda, MD, USA). Sex was determined at birth, and confirmed by abdominal examination at sacrifice. This
520 animal model is similar to the human in that males are more affected and, as such, only male OF1 pups were used,
521 as female OPCs maturation is not altered (Hagberg et al., 2015). IL1B injections were performed as described
522 (Favrais et al., 2011; Krishnan et al., 2017). Five µL volume of phosphate-buffered saline (PBS) containing
523 10µG/kG/injection of recombinant mouse IL1B (R&D Systems, Minneapolis, MN) or of PBS alone (control) was
524 injected intraperitoneally (i.p.) twice a day on days P1 to P4 and once a day, on day P5 (see Figure 1). Pups were
525 sacrificed four hours after the morning injection of IL1B at P3 or P5, and at a similar time at P9, or P10. ATAC-Seq
526 data were produced from 3 independent biological replicates for each condition (PBS or IL1B; Figure 1). Microarray
527 data were produced from 6 independent biological replicates for each condition (PBS or IL1B; Figure 1), using the
528 same animals that were also analysed for CD11B+ microarrays (Krishnan et al., 2017).

529

530 **O4+ and CD11B+ microglial magnetic activated cell-sorting in mouse**

531 O4+ cells were isolated at P3, P5, P9, or P10 by Magnetic Activated Cell Sorting (MACS, Miltenyi Biotec,
532 Bergisch Gladbach, Germany), according to the manufacturer's protocol and as previously described (Schang et al.,
533 2014). Briefly, brains were collected without cerebellum and olfactory bulbs, pooled (3 brains per sample) and
534 dissociated using the Neural Tissue Dissociation Kit containing papain. O4 + cells were then enriched by MACS, using
535 the anti-O4 MicroBeads. For microarray and RT-qPCR analysis, the eluted isolated cells were centrifuged for 5 min
536 at 600g and conserved at -80°C. CD11B+ microglial cells were isolated as described (Krishnan et al., 2017). The
537 unlabeled fraction mainly contained astrocytes (see Figure S1A). For the ATAC-seq experiment, 50,000 cells were
538 immediately lysed and their nuclei submitted to Tn5 activity. The purity of the eluted O4-positive fraction was
539 verified using qRT-PCR for Myelin Basic Protein (*Mbp*), ionizing calcium binding adapter protein (*Iba1*), glial fibrillary
540 acid protein (*Gfap*) and neuronal nuclear antigen mRNAs (*NeuN*; Figure S1A). Comparable numbers of O4+ OPCs
541 from control (PBS) and treated (IL1B) samples were collected (1.12×10^6+/- 0.12×10^6 cells per sample).

542

543 **OPC culture and differentiation**

544 OPCs were prepared from newborn OF1 mice as described (McCarthy and de Vellis, 1980; Pansiot et al.,
545 2016). In brief, forebrain cortices were removed from postnatal day 0–2 mouse pups and freed from meninges.
546 Minced tissues were enzymatically digested with 0.125% trypsin (Sigma) and 0,0025% DNase I (Sigma) for 15 min
547 at 37°C and then mechanically dissociated. Cells were filtered through a 100-µm-pore-size cell strainer (BD),
548 centrifuged 10 min at 1800 rpm, resuspended in minimum essential Eagle's medium (Sigma) supplemented with
549 10% FBS (Gibco), 1% Glutamax (Gibco), 1% penicillin-streptomycin (P/S) solution (Sigma), and 0.5% glucose and
550 plated in T75 flasks at a density of $2 \times 10^5/cm^2$. Mixed glial cell cultures were grown until confluence for 9-11 days
551 (medium was replaced every 48-72h) and shaken for 1.5 h at 260 rpm to detach microglia. These detached microglia
552 were then collected and removed together with the media. Remaining cells were shaken for additional 18h to
553 detach the OPCs from the astrocyte base layer, and were simultaneously treated with 100 µg/ml liposomal
554 clodrosome suspension (Clodrosome®, Encapsula Nanosciences, Brentwood, USA) which selectively eliminates any
555 residual microglia. The detached OPC cell suspension was filtered through a 20-µM-pore-size filter (Millipore) and
556 incubated in an untreated Petri dish for 10 min at 37°C to allow attachment of any remaining microglia. Purified
557 OPCs were then seeded onto poly-D-lysine-coated 12-multiwell plates at a density of $3 \times 10^4/cm^2$ in OPC
558 proliferation medium composed of Neurobasal medium (Gibco), 2% B21 (Miltenyi biotec), 1% P/S (Sigma) and 1%
559 Glutamax (Gibco), supplemented with growth factors consisting in 10nG/mL FGFα (Sigma) and 10nG/mL PDGFα
560 (Sigma). After 72h, OPC differentiation was initiated by growth factor withdrawal and addition of 40 nG/mL of T3
561 (Sigma). At the same time, OPCs were treated with 50nG/mL IL1B (R&D Systems, Minneapolis, MN) or PBS for 4h,
562 treatment was removed, new media provided and cells were grown in differentiation medium until 72h (Figure 4C).

563

564 **Oli-neu cell line culture and differentiation**

565 The immortalized murine OPC cell line, Oli-neu, was kindly provided by Dr Sheila Harroch (Pasteur Institute,
566 Paris, France). Oli-neu was established from OPC-enriched murine primary cultures from E16 brains transformed
567 with a provirus containing the oncogene *T-Neu* (Jung et al., 1995). Various differentiation protocols have been
568 established, among which treatment with PD174265, a selective inhibitor of the activity of Epidermal Growth Factor
569 receptor (ErbB) tyrosine kinase, has been shown to induce MBP expression (Gobert et al., 2009). These cells were
570 cultured in Dulbecco's modified Eagle's minimum essential medium (DMEM) containing Glutamax 1X and high
571 glucose (4.5 G/L; Gibco 31966), supplemented with 1 mG/mL insulin (Sigma), N2 supplement (Gibco), 100 µG/mL
572 T4 and T3 (Sigma), 1% horse serum (Gibco), and 1% P/S (Sigma). At confluence, the cells were mechanically
573 detached and seeded in 12-multiwell plates at a density of 3 x 10^4 cells/cm². After 24h, differentiation was induced
574 by addition of 1µM PD174265 (ChemCruz) diluted in DMSO at 1 mM. Medium was replaced after 48h and
575 differentiation was stopped after 72h (Figure 6B,C, Figure S1E).

576

577 **RT-qPCR analysis and Luminex assay**

578 Preparation of samples for quantitative reverse-transcriptase polymerase-chain reaction (qRT-PCR), primer
579 design PCR protocol and luminex assay were similar to that previously described (Chhor et al., 2013). Primer
580 sequences are given in Table S11. *Gapdh* (glyceraldehyde-3-phosphate dehydrogenase gene) and *Rpl13* (Ribosomal
581 Protein L13) were chosen to standardize the quantitative experiments based on reference gene suitability testing.

582

583 **ATAC-Seq analysis in O4+ OPCs**

584 ATAC-seq protocol was performed as described (Buenrostro et al., 2013) with slight modifications. In brief,
585 cells were immediately lysed after cell sorting and a total of 50,000 nuclei were subjected to Tn5-mediated
586 transposition for 30 min, resulting in 'tagmented' DNA fragments. Tagmented DNA was purified on MinElute colums
587 (Qiagen) and amplified/tagged in two steps using NEBnext High-Fidelity 2x PCR master mix (New England Biolabs).
588 Amplified DNA was purified twice with 1.8 volumes of NucleoMag NGS Clean-up and Size Select beads (Macherey
589 Nagel). DNA was quantified using the Qubit dsDNA HS Assay Kit and the quality of each library determined on Agilent
590 2100 Bioanalyzer DNA High Sensitivity ChIPs. Libraries demonstrating appropriate nucleosomal profiles were
591 multiplexed and subjected to Illumina NextSeq500 sequencing (IGenSeq Platform, ICM, Paris, France). Fastq files
592 are available in Dataset S1. The main steps of sequence analyses are summarized in Figure S2B and detailed on the
593 jupyter notebook available in supplemental information. After quality controls (Fastqc and Trimmomatic 0.33),
594 reads were aligned on the mm10 genome with Bowtie 2 (Galaxy tool version 2.3.4.1 (Afgan et al., 2016); default
595 parameters; Table S1; Figure S2B). Peak calling was performed with MACS2.2.0; default parameters; q<0.05)
596 separately for the two conditions, using a pooled (n=3) bam file of control samples and a pooled (n=3) bam file of
597 IL1B samples. The two resulting bed files were merged and, after removing the mm10 blacklist
598 (http://mitra.stanford.edu/kundaje/akundaje/release/blacklists/mm10-mouse/mm10.blacklist.bed.gz), 213,246
599 DNA regions (peaks) significantly detected in at least one condition were delimitated (Table S2). The number of
600 reads was determined in each peak for each sample using Bedtools coverage (version 2.19.1) and normalized to the
601 library sizes. Principal component analysis was performed on log transformed read count values of the top 500 most
602 variable peaks, using the prcomp function in R. Differential peak detection between the three PBS and the three
603 IL1B samples was performed with the Bioconductor software package EdgeR (3.22.3; Robinson et al., 2010), using
604 R studio (0.98.1103; http://www.rstudio.com). Statistical comparison was performed using the exact test function
605 followed by False Discovery Rate (FDR) determination by the Benjamini-Hochberg method. Raw data are available
606 under SRA BIOPROJECT accession # PRJNA540409.

607

608 **Linking of HAEC and OPC ATAC-Seq datasets**

609 We used a public ATAC-Seq dataset of human aortic endothelial cells (HAECs; Hogan et al., 2017; NCBI Gene
610 Expression Omnibus; accession no: GSE89970) and processed the raw reads (using the hg19 reference genome) to
611 obtain a set of peaks. Both sets of peaks (control and IL1B-treated samples) were annotated using HOMER's

612 annotatePeaks function. Next, HAEC peaks were matched to mouse OPC peaks through gene annotations, by taking
613 only those peaks annotated with matching orthologous genes (only 1-to-1 orthology was considered). Matching
614 was further restricted to promoter regions (peaks with a relative maximum distance of 2kb from the TSS). In order
615 to ensure that peaks were true matches, this set was further restricted to a relative distance of 500 bp from each
616 other in relation to the TSS. Using this approach, a total of 7,739 peaks were matched between the HAEC and OPC
617 datasets, including 100 peaks identified as differential in the HAEC dataset using DESeq2. Next, the number of reads
618 mapped to matched peaks were obtained by counting the number of reads at the summit ± 50bp using the
619 featureCounts package of the Subread software (v1.6.0) and the counts were normalized against the total number
620 of reads present in all matched peaks and converted into reads per million. Normalized read number distributions
621 of the two datasets were compared using the one-sample Wilcoxon rank test with continuity correction.
622
623 **Microarrays of mouse O4+ OPC gene expression and data preprocessing**
624 Microarray analysis was performed on six control and six IL1B samples (O4+ cells isolated at P5 after *in*
625 *vivo* PBS or IL1B treatment) using Agilent Whole Mouse Genome Oligo Microarrays 8x60K (Agilent). Raw data are
626 available in Dataset S2. All the steps, from RNA extraction to statistical analysis, were performed by Miltenyi Biotec,
627 as previously described (McCarthy and de Vellis, 1980). In brief, intensity data were subjected to quantile
628 normalization, unpaired t-tests (equal variance) were conducted to compare intensities between the two groups
629 for each probe and p-values were adjusted through FDR determination by the Benjamini-Hochberg method. Fold
630 changes correspond to the median ratios (median[IL1B]/median[PBS]). When FC<1, the FC was expressed as a
631 negative value using the formula FC(neg)=-1/FC. For example, if FC=0.5, the indicated FC is -2. Probes with FDR
632 <0.05 were considered significant. An additional fold change (FC) threshold was chosen at +/- 1.5 (corresponding to
633 FC>1.5 and <0.666).
634
635 **Heat map representation**
636 Heat maps were created using Morpheus (https://software.broadinstitute.org/morpheus). The Log2
637 median-centered data were visualized using a fixed (nonrelative) color pattern. The color scales are indicated on
638 each heatmap. Rows and columns were submitted to hierarchical clustering with the following criteria: metric =
639 one minus Pearson correlation, linkage method = average.
640
641 **GO-term enrichment analysis**
642 GO-term Biological Pathway enrichment was done using David 6.8 (Huang et al., 2009a; Huang et al.,
643 2009b).
644
645 **TFBS motif enrichment analysis, and TF footprint analysis**
646 The 213,246 significant peaks detected by MACS2 in at least one condition (PBS or IL1B) were annotated
647 with the *HOMER annotatePeaks* function. The list was restricted to the peaks located between -8000 and +8000 bp
648 from the closest TSS ("TSS-All" list). Among this list, peaks were selected, which were annotated with a gene name
649 and for which the gene expression was modulated in the microarray analysis (FDR<0.05 and FC>1.5 or <-1.5). The
650 full list of peaks and lists restricted to up or down-regulated genes were submitted to motif enrichment analysis
651 using *HOMER FindMotifsGenome* with the options "-size given" and "-mask". The "TSS-All" list was used as
652 background. Six motifs corresponding to the top 5 motifs enriched in the full list of peaks (ISRE, IRF1, IRF2, Nfkb-
653 p65 and PGR, Figure S5B) and the 15th motif enriched in the list restricted to up-regulated genes (PU1:IRF8, Figure
654 S5B) were localized in the full list of peaks (UP+DOWN) with *HOMER FindMotifs*. For each of these motifs, the
655 average profile of Tn5 activity was visualized using *pyDNAse* dnase_average_profile.py; Piper et al., 2013). This
656 profiling was performed using a pooled bam file of PBS samples, or a pooled bam file of IL1B samples separately,
657 and a pooled bam file of the two conditions ("both") together.

658 **Testing for enrichment of paired motifs**

659 2319 ATAC-Seq peaks corresponding to 1266 upregulated genes (886 different gene names) and 946 ATAC-
660 seq peaks corresponding to 454 downregulated (336 different gene names) were tested for significantly enriched
661 pairs of TFBS relative to a universe containing all the peaks located +/- 8 kb around the closest TSS. For each
662 individual motif from the homer database, all peaks in the universe were ranked by motif occupancy using a
663 binomial score. Then for every possible pair of motifs, peaks containing both motifs were identified using the
664 overlap between top 5000 ranked peaks for each of the individual motifs. A hypergeometric test was used to
665 calculate the enrichment score (p-value) for the overlap between each test set and the peaks containing both
666 motifs. The resulting p-values were corrected using the Benjamini-Hochberg correction.
667
668 **Statistical analysis**
669 All *in vivo* and *in vitro* experiments were performed using an alternating treatment allocation. All analyses
670 were performed by an experimenter blinded to the treatment groups. The results of qRT-PCR and Luminex analyses
671 are expressed as mean +/- SEM of at least four independent experiments; the number of analysed samples is
672 indicated in the figure legends or on the graphs. Statistical analysis was done using the non-parametric Mann-
673 Whitney t-test with Graphpad 5.0 software (San Diego, CA, USA) or two-way ANOVA followed by Bonferroni - Post
674 Hoc Test as indicated in each figure legend. Significance is shown on the graphs (*, $p < 0.05$; **, $p < 0.01$; ***, $p <$
675 0.001). Specific statistical analyses for ATAC-seq and microarray analyses are detailed in the dedicated sections of
676 Material and Methods. The significance of intersection between the two datasets was evaluated by hypergeometric
677 test (Phyper function) in R studio.
678

679 **REFERENCES**

680 Abane, R., and Mezger, V. (2010). Roles of heat shock factors in gametogenesis and development. FEBS J. *277*,
681 4150–4172.

682 Afgan, E., Baker, D., van den Beek, M., Blankenberg, D., Bouvier, D., Čech, M., Chilton, J., Clements, D., Coraor, N.,
683 Eberhard, C., et al. (2016). The Galaxy platform for accessible, reproducible and collaborative biomedical analyses:
684 2016 update. Nucleic Acids Res. *44*, W3–W10.

685 Balabanov, R., Strand, K., Goswami, R., McMahon, E., Begolka, W., Miller, S.D., and Popko, B. (2007). Interferon-
686 gamma-oligodendrocyte interactions in the regulation of experimental autoimmune encephalomyelitis. J.
687 Neurosci. Off. J. Soc. Neurosci. *27*, 2013–2024.

688 Ball, G., Boardman, J.P., Rueckert, D., Aljabar, P., Arichi, T., Merchant, N., Gousias, I.S., Edwards, A.D., and
689 Counsell, S.J. (2012). The effect of preterm birth on thalamic and cortical development. Cereb. Cortex N. Y. N 1991
690 *22*, 1016–1024.

691 Barnett, M.L., Tusor, N., Ball, G., Chew, A., Falconer, S., Aljabar, P., Kimpton, J.A., Kennea, N., Rutherford, M.,
692 David Edwards, A., et al. (2018). Exploring the multiple-hit hypothesis of preterm white matter damage using
693 diffusion MRI. NeuroImage Clin. *17*, 596–606.

694 Billiards, S.S., Haynes, R.L., Folkerth, R.D., Borenstein, N.S., Trachtenberg, F.L., Rowitch, D.H., Ligon, K.L., Volpe,
695 J.J., and Kinney, H.C. (2008). Myelin abnormalities without oligodendrocyte loss in periventricular leukomalacia.
696 Brain Pathol. Zurich Switz. *18*, 153–163.

697 Bokobza, C., Van Steenwinckel, J., Mani, S., Mezger, V., Fleiss, B., and Gressens, P. (2019). Neuroinflammation in
698 preterm babies and autism spectrum disorders. Pediatr. Res. *85*, 155–165.

699 Buenrostro, J.D., Giresi, P.G., Zaba, L.C., Chang, H.Y., and Greenleaf, W.J. (2013). Transposition of native chromatin
700 for fast and sensitive epigenomic profiling of open chromatin, DNA-binding proteins and nucleosome position.
701 Nat. Methods *10*, 1213–1218.

702 Buenrostro, J.D., Wu, B., Chang, H.Y., and Greenleaf, W.J. (2015). ATAC-seq: A Method for Assaying Chromatin
703 Accessibility Genome-Wide. Curr. Protoc. Mol. Biol. *109*, 21.29.1-21.29.9.

704 Cahoy, J.D., Emery, B., Kaushal, A., Foo, L.C., Zamanian, J.L., Christopherson, K.S., Xing, Y., Lubischer, J.L., Krieg,
705 P.A., Krupenko, S.A., et al. (2008). A transcriptome database for astrocytes, neurons, and oligodendrocytes: a new
706 resource for understanding brain development and function. J. Neurosci. Off. J. Soc. Neurosci. *28*, 264–278.

707 Cardona, A.E., Li, M., Liu, L., Savarin, C., and Ransohoff, R.M. (2008). Chemokines in and out of the central nervous
708 system: much more than chemotaxis and inflammation. J. Leukoc. Biol. *84*, 587–594.

709 Chang, Y., Ostling, P., Akerfelt, M., Trouillet, D., Rallu, M., Gitton, Y., El Fatimy, R., Fardeau, V., Le Crom, S.,
710 Morange, M., et al. (2006). Role of heat-shock factor 2 in cerebral cortex formation and as a regulator of p35
711 expression. Genes Dev. *20*, 836–847.

712 Chhor, V., Le Charpentier, T., Lebon, S., Oré, M.-V., Celador, I.L., Josserand, J., Degos, V., Jacotot, E., Hagberg, H.,
713 Sävman, K., et al. (2013). Characterization of phenotype markers and neuronotoxic potential of polarised primary
714 microglia in vitro. Brain. Behav. Immun. *32*, 70–85.

715 Cuomo, F., Coppola, A., Botti, C., Maione, C., Forte, A., Scisciola, L., Liguori, G., Caiafa, I., Ursini, M.V., Galderisi, U.,
716 et al. (2018). Pro-inflammatory cytokines activate hypoxia-inducible factor 3α via epigenetic changes in
717 mesenchymal stromal/stem cells. Sci. Rep. *8*, 5842.

718 Delobel-Ayoub, M., Arnaud, C., White-Koning, M., Casper, C., Pierrat, V., Garel, M., Burguet, A., Roze, J.-C., Matis,
719 J., Picaud, J.-C., et al. (2009). Behavioral problems and cognitive performance at 5 years of age after very preterm
720 birth: the EPIPAGE Study. Pediatrics *123*, 1485–1492.

721 Deverman, B.E., and Patterson, P.H. (2009). Cytokines and CNS development. Neuron *64*, 61–78.

722 Espín-Palazón, R., and Traver, D. (2016). The NF-κB family: Key players during embryonic development and
723 HSC emergence. Exp. Hematol. *44*, 519–527.

724 Favrais, G., van de Looij, Y., Fleiss, B., Ramanantsoa, N., Bonnin, P., Stoltenburg-Didinger, G., Lacaud, A., Saliba, E.,
725 Dammann, O., Gallego, J., et al. (2011). Systemic inflammation disrupts the developmental program of white
726 matter. Ann. Neurol. *70*, 550–565.

727 Gobert, R.P., Joubert, L., Curchod, M.-L., Salvat, C., Foucault, I., Jorand-Lebrun, C., Lamarine, M., Peixoto, H.,
728 Vignaud, C., Frémaux, C., et al. (2009). Convergent functional genomics of oligodendrocyte differentiation
729 identifies multiple autoinhibitory signaling circuits. Mol. Cell. Biol. *29*, 1538–1553.

730 Gomez-Pastor, R., Burchfiel, E.T., and Thiele, D.J. (2018). Regulation of heat shock transcription factors and their
731 roles in physiology and disease. Nat. Rev. Mol. Cell Biol. *19*, 4–19.

732 Green, B., Bouchier, C., Fairhead, C., Craig, N.L., and Cormack, B.P. (2012). Insertion site preference of Mu, Tn5,
733 and Tn7 transposons. Mob. DNA *3*, 3.

734 Hagberg, H., Mallard, C., Ferriero, D.M., Vannucci, S.J., Levison, S.W., Vexler, Z.S., and Gressens, P. (2015). The role
735 of inflammation in perinatal brain injury. Nat. Rev. Neurol. *11*, 192–208.

736 Halder, R., Hennion, M., Vidal, R.O., Shomroni, O., Rahman, R.-U., Rajput, A., Centeno, T.P., van Bebber, F.,
737 Capece, V., Garcia Vizcaino, J.C., et al. (2016). DNA methylation changes in plasticity genes accompany the
738 formation and maintenance of memory. Nat. Neurosci. *19*, 102–110.

739 Heinz, S., Benner, C., Spann, N., Bertolino, E., Lin, Y.C., Laslo, P., Cheng, J.X., Murre, C., Singh, H., and Glass, C.K.
740 (2010). Simple combinations of lineage-determining transcription factors prime cis-regulatory elements required
741 for macrophage and B cell identities. Mol. Cell *38*, 576–589.

742 Hogan, N.T., Whalen, M.B., Stolze, L.K., Hadeli, N.K., Lam, M.T., Springstead, J.R., Glass, C.K., and Romanoski, C.E.
743 (2017). Transcriptional networks specifying homeostatic and inflammatory programs of gene expression in human
744 aortic endothelial cells. ELife *6*.

745 Huang, D.W., Sherman, B.T., and Lempicki, R.A. (2009a). Systematic and integrative analysis of large gene lists
746 using DAVID bioinformatics resources. Nat. Protoc. *4*, 44–57.

747 Huang, D.W., Sherman, B.T., and Lempicki, R.A. (2009b). Bioinformatics enrichment tools: paths toward the
748 comprehensive functional analysis of large gene lists. Nucleic Acids Res. *37*, 1–13.

749 Jana, M., and Pahan, K. (2005). Redox regulation of cytokine-mediated inhibition of myelin gene expression in
750 human primary oligodendrocytes. Free Radic. Biol. Med. *39*, 823–831.

751 Jung, M., Krämer, E., Grzenkowski, M., Tang, K., Blakemore, W., Aguzzi, A., Khazaie, K., Chlichlia, K., von
752 Blankenfeld, G., and Kettenmann, H. (1995). Lines of murine oligodendroglial precursor cells immortalized by an
753 activated neu tyrosine kinase show distinct degrees of interaction with axons in vitro and in vivo. Eur. J. Neurosci.
754 *7*, 1245–1265.

755 Krishnan, M.L., Van Steenwinckel, J., Schang, A.-L., Yan, J., Arnadottir, J., Le Charpentier, T., Csaba, Z., Dournaud,
756 P., Cipriani, S., Auvynet, C., et al. (2017). Integrative genomics of microglia implicates DLG4 (PSD95) in the white
757 matter development of preterm infants. Nat. Commun. *8*, 428.

758 Kumar, H., Lim, J.-H., Kim, I.-S., and Choi, D.-K. (2015). Differential regulation of HIF-3α in LPS-induced BV-2
759 microglial cells: Comparison and characterization with HIF-1α. Brain Res. *1610*, 33–41.

760 Laguesse, S., Creppe, C., Nedialkova, D.D., Prévot, P.-P., Borgs, L., Huysseune, S., Franco, B., Duysens, G., Krusy, N.,
761 Lee, G., et al. (2015). A Dynamic Unfolded Protein Response Contributes to the Control of Cortical Neurogenesis.
762 Dev. Cell *35*, 553–567.

763 Leviton, A., and Gressens, P. (2007). Neuronal damage accompanies perinatal white-matter damage. Trends
764 Neurosci. *30*, 473–478.

765 Mancino, A., Termanini, A., Barozzi, I., Ghisletti, S., Ostuni, R., Prosperini, E., Ozato, K., and Natoli, G. (2015). A
766 dual cis-regulatory code links IRF8 to constitutive and inducible gene expression in macrophages. Genes Dev. *29*,
767 394–408.

768 Matcovitch-Natan, O., Winter, D.R., Giladi, A., Vargas Aguilar, S., Spinrad, A., Sarrazin, S., Ben-Yehuda, H., David,
769 E., Zelada González, F., Perrin, P., et al. (2016). Microglia development follows a stepwise program to regulate
770 brain homeostasis. Science *353*, aad8670.

771 McCarthy, K.D., and de Vellis, J. (1980). Preparation of separate astroglial and oligodendroglial cell cultures from
772 rat cerebral tissue. J. Cell Biol. *85*, 890–902.

773 Moyon, S., Dubessy, A.L., Aigrot, M.S., Trotter, M., Huang, J.K., Dauphinot, L., Potier, M.C., Kerninon, C., Melik
774 Parsadaniantz, S., Franklin, R.J.M., et al. (2015). Demyelination causes adult CNS progenitors to revert to an
775 immature state and express immune cues that support their migration. J. Neurosci. Off. J. Soc. Neurosci. *35*, 4–20.

776 Pansiot, J., Pham, H., Dalous, J., Chevenne, D., Colella, M., Schwendimann, L., Fafouri, A., Mairesse, J., Moretti, R.,
777 Schang, A.-L., et al. (2016). Glial response to 17β-estradiol in neonatal rats with excitotoxic brain injury. Exp.
778 Neurol. *282*, 56–65.

779 Piper, J., Elze, M.C., Cauchy, P., Cockerill, P.N., Bonifer, C., and Ott, S. (2013). Wellington: a novel method for the
780 accurate identification of digital genomic footprints from DNase-seq data. Nucleic Acids Res. *41*, e201.

781 Rangon, C.-M., Schang, A.-L., Van Steenwinckel, J., Schwendimann, L., Lebon, S., Fu, T., Chen, L., Beneton, V.,
782 Journiac, N., Young-Ten, P., et al. (2018). Myelination induction by a histamine H3 receptor antagonist in a mouse
783 model of preterm white matter injury. Brain. Behav. Immun. *74*, 265–276.

784 Robinson, M.D., McCarthy, D.J., and Smyth, G.K. (2010). edgeR: a Bioconductor package for differential expression
785 analysis of digital gene expression data. Bioinforma. Oxf. Engl. *26*, 139–140.

786 Schang, A.-L., Van Steenwinckel, J., Chevenne, D., Alkmark, M., Hagberg, H., Gressens, P., and Fleiss, B. (2014).
787 Failure of thyroid hormone treatment to prevent inflammation-induced white matter injury in the immature
788 brain. Brain. Behav. Immun. *37*, 95–102.

789 Schang, A.-L., Sabéran-Djoneidi, D., and Mezger, V. (2018). The impact of epigenomic next-generation sequencing
790 approaches on our understanding of neuropsychiatric disorders. Clin. Genet. *93*, 467–480.

791 Shiow, L.R., Favrais, G., Schirmer, L., Schang, A.-L., Cipriani, S., Andres, C., Wright, J.N., Nobuta, H., Fleiss, B.,
792 Gressens, P., et al. (2017). Reactive astrocyte COX2-PGE2 production inhibits oligodendrocyte maturation in
793 neonatal white matter injury. Glia *65*, 2024–2037.

794 Stadhouders, R., Vidal, E., Serra, F., Di Stefano, B., Le Dily, F., Quilez, J., Gomez, A., Collombet, S., Berenguer, C.,
795 Cuartero, Y., et al. (2018). Transcription factors orchestrate dynamic interplay between genome topology and
796 gene regulation during cell reprogramming. Nat. Genet. *50*, 238–249.

797 Van Steenwinckel, J., Schang, A.-L., Krishnan, M.L., Degos, V., Delahaye-Duriez, A., Bokobza, C., Csaba, Z., Verdonk,
798 F., Montané, A., Sigaut, S., et al. (2019). Decreased microglial Wnt/β-catenin signalling drives microglial pro-
799 inflammatory activation in the developing brain. Brain J. Neurol. *142*, 3806–3833.

800 Vihervaara, A., Mahat, D.B., Guertin, M.J., Chu, T., Danko, C.G., Lis, J.T., and Sistonen, L. (2017). Transcriptional
801 response to stress is pre-wired by promoter and enhancer architecture. Nat. Commun. *8*, 255.

802 Vihervaara, A., Duarte, F.M., and Lis, J.T. (2018). Molecular mechanisms driving transcriptional stress responses.
803 Nat. Rev. Genet. *19*, 385–397.

804 Volpe, J.J. (2009). Brain injury in premature infants: a complex amalgam of destructive and developmental
805 disturbances. Lancet Neurol. *8*, 110–124.

806 Volpe, J.J. (2011). Systemic inflammation, oligodendroglial maturation, and the encephalopathy of prematurity.
807 Ann. Neurol. *70*, 525–529.

808 Wang, L., Yang, H., Zang, C., Dong, Y., Shang, J., Chen, J., Wang, Y., Liu, H., Zhang, Z., Xu, H., et al. (2020). CXCR2
809 antagonism promotes oligodendrocyte precursor cell differentiation and enhances remyelination in a mouse
810 model of multiple sclerosis. Neurobiol. Dis. *134*, 104630.

811 Yanai, H., Negishi, H., and Taniguchi, T. (2012). The IRF family of transcription factors: Inception, impact and
812 implications in oncogenesis. Oncoimmunology *1*, 1376–1386.

813 Zeis, T., Enz, L., and Schaeren-Wiemers, N. (2016). The immunomodulatory oligodendrocyte. Brain Res. *1641*,
814 139–148.

815 Zhang, Y., Liu, T., Meyer, C.A., Eeckhoute, J., Johnson, D.S., Bernstein, B.E., Nusbaum, C., Myers, R.M., Brown, M.,
816 Li, W., et al. (2008). Model-based analysis of ChIP-Seq (MACS). Genome Biol. *9*, R137.

817
818

819 **LEGENDS OF FIGURES**

820 **Figure 1. Experimental strategy.** (see also Figure S1). Previously validated mouse model of encephalopathy of
821 prematurity in which we mimic the systemic and neuroinflammatory insults as undergone by human infants from
822 approximately [23-32]-week gestational age equivalent. Neuroinflammation is induced *via* i.p. IL1B from postnatal
823 days 1 to 5, and this leads to OPC maturation blockade, defective myelination, and behavioral anomalies as seen
824 clinically (Favrais et al., 2011). O4+ OPCs (green circles) were isolated from P5 pup cortices by MACS and genome-
825 wide chromatin accessibility was explored by ATAC-Seq (lower, left panel): the enzymatic severing of the DNA by
826 the transposome (Tn5 transposase, loaded with adapters *in vitro*; green and orange) allows « tagmentation » of
827 DNA template, to fragments tagged with adapters. In parallel (lower, right panel), comparative transcriptomic
828 analysis was performed using Agilent mouse whole genome microarray.

829 **Figure 2. The epigenome of OPCs is globally preserved after IL1B treatment (ATAC-Seq analysis).** (see Figure S1,
830 S2 and S3)
831 (**A**) PCA analysis of log normalized read counts falling within ATAC-seq chromatin peaks from OPCs from control
832 (PBS) or neuroinflammation-exposed (IL1B injections); total number of peaks, 213,246.
833 (**B**) Scatter plot representing the dispersion (fold change) of peaks in relation to the number of tn5 cuts per million
834 (logCPM), for each individual analyzed peak across 3 PBS samples and 3 IL1B samples. The 524 peaks showing
835 significant differences between IL1B and PBS conditions are indicated in red, with 391 peaks corresponding to
836 increased and 133 peaks to decreased chromatin accessibility, with FDR < 0.05.
837 (**C**) Heat map visualization of the 524 opening (yellow) or closing (blue) peaks in control (PBS) and
838 neuroinflammation-exposed (IL1B injected) conditions.
839 (**D**) Examples of peaks showing increased or unmodified chromatin accessibility: (Upper panel) the peaks located at
840 the most downstream position in the *Hif3a gene* (*Hypoxia inducible factor 3 alpha subunit*) show increased
841 chromatin accessibility in neuroinflammation context) Magnification of this region is illustrated in the lower panel).
842 In contrast, peaks located in the middle of the *Hif3a* gene show no significant changes in chromatin accessibility
843 (Upper panel).
844 (**E**) Example of peak showing reduced chromatin accessibility: peaks within the *Cwc22* gene (encoding the
845 spliceosome-associated protein 22).
846 (**F**) Example of peaks in genes encoding cytokines and chemokines, showing no statistically relevant modification of
847 chromatin accessibility.

848 **Figure 3. Major transcriptomic impact of neuroinflammation on the immune/inflammatory pathway in O4+ OPCs.**
849 (see Figures S1, S4A,B and Table S4)**.** Microarray analysis comparing gene expression in isolated O4+ OPCs from six
850 independent control (PBS) and six independent neuroinflammation-exposed cortices (IL1B; Figure 1).
851 (**A**) ***Heat map of genes with altered expression upon IL1B exposure.*** A fold-change (FC) threshold of +/-1.5 was
852 chosen, with FDR < 0.05. Total number of probes corresponding to IL1B-induced disturbances in gene expression:
853 2571, corresponding to 1719 genes. Total number of probes corresponding to the 1266 upregulated genes: 1872.
854 Total number of probes corresponding to the 454 downregulated genes: 699. Heatmap color scale: log2 [-2.0;+2.0].
855 (**B**) ***The top5 GO-terms of up-regulated genes corresponds to the immune system and inflammatory response***
856 ***pathways***. GO-terms as a table with the number of upregulated genes per GO-term, p-values, and FDR.
857 (**C**) ***Heat map of the genes belonging to the top5 GO-terms,*** 315 probes corresponding to 262 genes. Heatmap
858 color scale: log2 [-2.0 ; +2.0].
859 (**D**) ***Validation of the alteration in gene expression for members of the GO-term "immune system and***
860 ***inflammatory response pathways" in O4+ OPCs using RT-qPCR***. Number of independent experiments: n=8 for all
861 genes, except for *Cxcl9*, *Cxcl10*, and *Il1r1* (n=7).*, $p < 0.05$; **, $p < 0.01$; ***, $p < 0.001$. Grey bars ligands; black bars:
862 receptors.

863

Figure 4. The production of cytokine and chemokine proteins by MACS-isolated O4+ OPCs is induced by neuroinflammation *in vivo* and *ex vivo.* (see Figures S1, S4C)

(**A**) ***Isolated O4+ OPCs and isolated CD11B+ microglial cells exhibit distinct induction profiles of immune/inflammatory gene expression in response to neuroinflammation.*** Heatmap comparison of the microarray data of the 262 upregulated genes of the immune/inflammatory pathway in isolated O4+ (described in Figure 3C) with the corresponding genes in CD11B+ microglial cells (Krishnan et al., 2017). Notably, these data where produced from cells originating from the same brains, at the same timepoint. Heatmap color scale of log2 [-2.0;+2.0].

(**B**) ***Unique signature for inflammatory gene expression in isolated O4+ OPCs, compared to CD11B+ microglia, and GLAST+ astrocytes***. Fold-change in the expression of genes of the immune and inflammatory pathways as detected by RT-qPCR analyses at different postnatal stages. mRNA levels are normalized to *Gapdh* for OPCs and astrocytes and *Rpl13* for microglia based on in-house reference gene testing. The numbers of independent experiments are indicated on each plot. *, $p < 0.05$; **, $p < 0.01$; ***, $p < 0.001$.

(**C**) ***Experimental design for ex vivo OPC culture, inflammatory exposure (IL1B), and differentiation*** (see Material and Methods).

(**D**) ***Protein detection and quantification*** (pG/mL) of the expression of interleukins (IL1B, IL6), cytokine C-C Motif Chemokine Ligand 2, 4, and 5 (CCL2, CCL3, CCL4, and CCL5) and chemokine C-X-C Motif Chemokine Ligand 2 (CXCL2) by Luminex. CTR, PBS exposure; IL1B, IL1B exposure. The dotted line represents the limit of detection for individual proteins in the assay. The numbers of independent experiments performed for each plot are indicated on each plot. *, $p < 0.05$; **, $p < 0.01$; ***, $p< 0.001$.

Figure 5. Major involvement of TFs of the immune and inflammatory pathways in O4+ OPCs. (see Figures S5 and S6)

(**A** and **B**) ***Crosstabulation of ATAC-Seq and microarray data*.**

(**A**) Number of genes differentially expressed and associated with all differentially accessible peaks/regions in O4+ OPCs isolated from neuroinflammation-exposed pups.

(**B**) Number of genes differentially expressed and associated with differentially accessible peaks/regions only located +/- 8 kb around their TSS in O4+ OPCs isolated from neuroinflammation-exposed pups.

(**C**) ***Co-localization of pairs of TF binding motifs in ATAC-Seq peaks of upregulated genes*.** Heat map of the paired motifs located in the 2319 ATAC-Seq peaks located within +/- 8 kb from the TSS of 1266 upregulated genes (corresponding to 886 different gene names), identified using paired motif analysis. Transcription factors (TF) names from MEME nomenclature on both axes. Statistically relevant co-occurrence of two different TFs is indicated by yellow to orange squares (multiple testing corrected log10 p-value). Examples of TF pairs are indicated IRF1-p50; *ISRE*-p65; PU.1-IRF8-p65; PU.1-iRF8-p50; PU.1-BATF; PU.1-FOSL2. Color code (TF names and arrows): red, pairing of PU.1-IRF8 with NFκB subunit binding motifs; purple, pairing of PU.1 with AP-1 family binding motifs; blue, pairing of NFKB binding motifs with *Isre* (IFN-stimulated response element); green, pairing of NFKB with IRF binding motifs.

(**D**) Chromatin accessibility footprints at TF motifs**.** Examples of average footprint profiles at TF motifs that were plotted at base pair resolution, located within accessible chromatin *loci* in <u>both</u> PBS and IL1B conditions, adjacent to differentially regulated genes (ALL; down and upregulated) using the Wellington software (Piper et al., 2013). Typical footprint profiles coincide with the center of the canonical motif for a given TF (indicated by brackets). Footprints for occupancy of IRF1, IRF2, *Isre,* and NFκB binding motifs are illustrated. Footprints showing occupancy by IRF1, IRF2, *Isre,* and NFκB on corresponding binding motifs are illustrated. Red and blue curves: + and - strand, respectively.

Figure 6. Constitutive expression of genes encoding cytokines and chemokines at early stages of normal (unstressed) O4+ OPC maturation. (see Figures S1E and S7).

(**A**) RT-qPCR analyses in P3, P5, and P10 O4+ OPCs. N= 5 to 6 independent experiments. Two-way ANOVA followed by Bonferroni - Post Hoc Test was performed: * and +, $p < 0.05$; ** and, ++ $p < 0.01$; ***, $p < 0.001$. *, **, or ***, correspond to comparison between PBS and IL1 conditions for a given postnatal stage; + (or ++), correspond to

911 comparison between P5 (or P10) to P3. (see Figure S7).
912 (**B** and **C**) ***The oligodendroglial cell line Oli-neu reproduces the constitutive expression of cytokine and chemokine***
913 ***gene at the immature state and its downregulation upon differentiation*** (see Figure S1E)
914 (**B**) Differentiation protocol of the Oli-neu cell line triggered by PD174265, a potent, cell-permeable inhibitor of the
915 tyrosine kinase activity of the epidermal growth factor receptor (EGFR)
916 (**C**) RT-qPCR analyses in the Oli-neu cell line before or after 72 hours of differentiation. This *in vitro* paradigm shows
917 the same pattern as O4+ OPCs, in terms of inflammatory mediator gene expression at the immature
918 (undifferentiated) state and decrease when maturating to myelin-producing oligodendrocytes. Numbers of
919 independent experiments are indicated on the graph bars. *, $p < 0.05$; **, $p < 0.01$. nd: not detected.

920 **Figure 7. Correlative upregulation of genes of the immune/inflammatory pathway and downregulation of the**
921 **myelination program in an oligodendroglial cell line upon inflammatory stimulus.** *Ex vivo* treatment of the Oli-neu
922 cell line by TFN-alpha reproduces the disturbances in gene expression that we observe in isolated O4+ OPCs upon
923 *in vivo* neuroinflammation. Illustrated here for the *Cnp*, *Mbp*, genes, and *Ccl2 and Cxcl10,* respectively. RT-qPCR
924 analyses (n = 6 independent experiments). Oli-neu cells were differentiated by 1 µM of PD174265 as in Figure 6C,D
925 (Gobert et al., 2009; see materials and methods), during 72h, in absence (T72 co) or in presence of 10 ng/ml TNFα
926 (T72 +TNFa). T_0: undifferentiated cells. Non parametric t-tests; ** $p< 0.01$.
927

928 **LEGENDS OF SUPPLEMENTAL FIGURES**

929 **Figure S1. Assessment of the purity of the isolated O4+ OPC population** (related to Figures 1-4,6).

930 (**A**) ***Quality assessment of the O4+ OPC cell purification process*** (relative to Figure 1) RT-qPCR experiments on the
931 O4+ OPC, CD11B+ microglia (MG; Krishnan et al., 2017; n=3 PBS samples and n=3 IL1B samples) and unlabeled cell
932 populations, showing that, in contrast to MG (CD11B+) and astrocytes (unlabeled), the population of O4+ OPCs used
933 in this study express the *Mbp* gene, whereas it exhibits very low mRNA levels of the microglia marker CD11 (encoded
934 by the *Itgam* gene), the astrocyte marker *Gfap*, or of the neuronal marker *NeuN*. Note that *NeuN* is very lowly
935 expressed, even in the unlabeled population, which mainly contains astrocytes, because neurons poorly survive our
936 MACS protocol.

937 **(B) *Distinct perturbations in gene expression profiles in isolated O4+ OPCs and CD11B+ MG, at P5 upon***
938 ***neuroinflammation*.** Heat maps of the overall comparison of neuroinflammation-induced transcriptomic changes.
939 (related to Figure 4). OP4+ OPCs exhibit profiles of transcriptomic modifications globally very different from that of
940 CD11B+ microglial cells (data by Krishnan et al., 2017). Notably, these cell populations were isolated from the same
941 animals at P5. Examples of genes encoding cytokines and chemokines are pointed out by rectangles. Most of them
942 are not upregulated in CD11B+ microglial cells at P5, in contrast to what happens in O4+ OPCs. Log2 Fold change ([-
943 2.0; +2.0]; IL1B/PBS)

944 (**C**,**D**) ***Distinct profiles of chromatin accessibility in genes specific for OPCs*** (our ATAC-seq data, green peaks; Figure
945 2 and Figure S2,3) ***and MG*** (ATAC-Seq data mining from (Matcovitch-Natan et al., 2016; red peaks).

946 (**E**) ***The oligodendroglial cell line Oli-neu reproduces the constitutive expression of cytokine and chemokine gene***
947 ***at the immature state and its downregulation upon differentiation observed along the maturation time-course.***
948 (relative to Figure 6B,C). RT-qPCR analyses in the Oli-neu cell line before or after 72 hours of differentiation triggered
949 by exposure (+) to conditioned medium (CM) from primary neuron culture.

950 **Figure S2. ATAC-Seq data quality control.** (related to Figure 2)

951 (**A**) ***Quality-control validation of OPC maturation arrest in the model.*** RT-qPCR analysis of the expression of
952 myelination and progenitor markers in OPCs. Myelin markers: *Mbp*, Myelin binding protein; *Mog*, Myelin
953 oligodendrocyte glycoprotein; *Mag*, Myelin-associated glycoprotein. *Plp1*, proteolipid protein 1, a transmembrane,
954 predominant component of myelin; *Cnp*, 2',3'-Cyclic Nucleotide 3' Phosphodiesterase, abundant protein in myelin
955 in the central nervous system. Progenitor (OPC) markers: *Id2*, Inhibitor of differentiation 2; *Pdgfra*, Platelet Derived
956 Growth Factor Receptor Alpha. Number of independent experiments: n = 7 for *Cnp*, *Mag*, and *Pdgfra*; and n = 15
957 for *Mbp*, *Mog*, and *Id2*. ns: not statistically significant; *, $p < 0.05$; ***, $p < 0.001$.

958 (**B**) ***Schematic representation of the bioinformatics and statistics workflow used for the analysis of ATAC-Seq data***
959 (**C**) ***Fragment-length distributions in ATAC-Seq samples***. Insert size distribution shows visible large periodicity of
960 the nucleosome-free, mononucleosomal and dinucleosomal fragments, as well as the expected ~10.4bp periodicity,
961 resulting from steric hindrance of the helical twist of the DNA on the nucleosome surface.

962 **Figure S3. The epigenome of OPCs is globally preserved after IL1B treatment (ATAC-Seq analysis)** (related to Figure
963 2)

964 (**A**) Multidimensional Scaling (MDS) plot of distances between the 3 PBS samples and the 3 IL1B samples, using
965 EdgeR.

966 (**B**) Scatter plots representing the dispersion (logfold change) as the number of tn5 cuts per million (logCPM), for
967 each individual analyzed peak (across 3 PBS samples and 3 IL1B samples). In red, peaks showing differential
968 chromatin accessibility with FDR < 0.05. The upper left plot is identical to Figure 2B and is included here for
969 comparison. Upper right, lower left, and lower right: scatter plots for analyses with permuted sample labels, created
970 by swapping of one of the PBS samples with one other IL1B samples or, vice-versa. Mixing PBS and IL1B samples led
971 to very reduced numbers of differential peaks, confirming that differential peaks found with correct sample labels
972 are not statistical artefacts

973 (**C**) Distribution of the total number of peaks and of the 524 differential open peaks (right-hand side) in various
974 genomic regions.

975 (**D**) GO analysis, using DAVID6.8 (Huang et al., 2009a; Huang et al., 2009b), using genes with TSS of genes that are
976 annotated with one or more differentially accessible chromatin regions (total of 524 ATAC-Seq peaks).
977
978 **Figure S4. The induction of cytokine and chemokine mRNA levels, upon IL1B exposure, is reproduced in MACS-**
979 **isolated *ex vivo* cultured OPCs during differentiation**. (related to Figure 3 and Figure 4C,D)
980 (**A**) ***Quality control of the samples used for microarray analysis.*** Relative expression, by microarray analysis, of
981 several myelination markers and Inhibitor of Differentiation *Id2* in O4+ OPCs at P5 (6 PBS samples and 6 IL1B
982 samples)
983 (**B**) ***GO analysis corresponding to the TOP-10 genes, which are downregulated upon IL1B treatment, using***
984 ***DAVID6.8***.
985 (**C**) ***Cultured O4+ OPCs express cytokine and chemokine genes***. RT-qPCR experiments on OPCs collected after 72h
986 of differentiation (see experimental design on Figure 4C). Number of independent experiments: n = 6 per condition
987 (PBS or IL1B). *, $p < 0.05$; **, $p < 0.01$; ***, $p < 0.01$.

988 **Figure S5. TFBS motifs identified in significant ATAC-seq peaks** adjacent to (**A**) all differentially regulated genes
989 (ALL) or (**B**) upregulated genes (UP), using HOMER known motifs. (related to Figure 5)

990 **Figure S6. Examples of chromatin accessibility footprint profiles at TF motifs**. (related to Figure 5).
991 (**A**) Average footprint profiles at transcription factor (TF) binding motifs plotted at base pair resolution, located
992 within accessible chromatin *loci* adjacent to any differentially regulated genes (down or upregulated) for the
993 following TF or binding sites: *Isre,* IRF1, IRF2, NFκB in PBS-treated or IL1B-treated samples, indicating that these TFs
994 might already bind DNA.
995 (**B**) Average footprints showing sharp internal spikes are suggestive of transposase insertion bias for PU.1-IRF8 or
996 PGR factors, from PBS-treated, IL1B-treated samples or from both conditions (PBS plus IL1B)..

997 **Figure S7. Constitutive expression of cytokines and chemokines by unstressed early maturating OPCs and**
998 **immune/inflammatory signature.** (related to Figure 6).
999 (**A**) ***Expected increase in the expression of genes associated with myelination between P5 and P10 in normal***
1000 ***conditions and expected impairment of this increase upon IL1B exposure***. RT-qPCR analyses in P3, P5, and P10 O4+
1001 OPCs. Note that in this set of experiments the downregulation of myelination genes was not observed at P5, a stage
1002 at which these genes only start to be expressed.
1003 (**B**) ***O4+ OPCs from naïve pups also constitutively express cytokine and chemokine genes***. RT-qPCR experiments
1004 comparing O4+ OPC from naïve (no injection), PBS-injected and IL1B-injected pups, showing that PBS injection does
1005 not induce expression of cytokines and chemokine genes, *per se*, since transcripts levels are equivalent in both PBS
1006 and naïve conditions, in contrast to what is observed upon IL1B treatment.
1007 (**C,D**) **Cross-species comparison confirms global similarities in the chromatin landscapes of HAEC and unstressed**
1008 **O4+ OPC datasets.**
1009 (**C**) Comparison of 100 peaks which were found to be differential in the HAEC (public) dataset upon IL1B treatment,
1010 among all (7739) matched peaks between human (HAEC) and mouse (OPCs) datasets. Reads were normalized for
1011 each set of peaks against the total number of reads present in all matched peaks and converted into reads per
1012 million. Distributions were compared using a one-sample Wilcoxon rank test.
1013 (**D**) Read number distribution of peaks upon IL1B treatment in the HAEC and OPC datasets. Reads were normalized
1014 for each set of peaks against the total number of reads present in the 7739 matched peaks and converted into RPM
1015 (read per million).
1016

1017 **LIST AND LEGENDS OF SUPPLEMENTAL INFORMATION**
1018 **TABLES:**
1019 **Table S1: Alignment statistics of ATAC-seq**
1020 The alignment statistics of the samples is in line with what is expected from ATAC-Seq samples. Losing in the
1021 region of 10% of reads to mitochondrial alignment is normal for this type of data.
1022
1023 **Table S2: Coordinates of the 213,246 peaks (mm10) detected in PBS and/or IL1B samples**
1024 MACS2 peak calling was run separately on PBS and IL1B pooled samples (n=3/group). The two resulting peak files
1025 (almost 200,000 peaks in each condition) were merged and the mm10 blacklist removed, leading to a list of 213,246
1026 peaks detected in at least one condition (mm10 coordinates).
1027
1028 **Table S3: List and annotation of the 524 differentially accessible peaks**
1029 Reads were counted in each of the 213,246 peaks (Table S2) for each sample individually (3 PBS and 3 IL1B samples).
1030 Comparison and statistical analysis with EdgeR (exact test and FDR by Benjamini-Hochberg method) identified 524
1031 peaks with differential accessibility (FDR<0.05). Peaks were annotated using HOMER annotatePeaks.
1032
1033 **Table S4: GO-term Biological Pathway analysis of the 524 differentially accessible peaks**
1034 GO-term Biological Pathway enrichment analysis was performed on the list of gene names (478) associated with
1035 the 524 peaks (Table S3) using David6.8.
1036
1037 **Table S5: List of the differentially expressed probes from the microarray analysis**
1038 Agilent microarray data from 6 PBS and 6 IL1B samples (O4+, P5) were submitted to t-test and FDR by Benjamini-
1039 Hochberg method. Probes with FDR<0.05 and FC>1.5 (or <-1.5) are listed in the table (Sheet 1). Up-regulated (Sheet
1040 2) and down-regulated (sheet 3) probes are also presented separately. Red flags (columns F and G) indicate the
1041 number of undetectable samples (0 means that all samples were detected). Red and green fold change values
1042 (column K) correspond to FC>2.0 and FC<-2.0, respectively. Individual values (N to Y columns) are normalized
1043 median-centered Log2 intensities.
1044
1045 **Table S6: GO-term Biological Pathway analysis of the UP and DOWN-regulated genes**
1046 GO-term Biological Pathway enrichment analysis was performed using David6.8 on significantly up-regulated (Sheet
1047 1) and down-regulated genes (Sheet 2) from the microarray analysis (Table S5).
1048
1049 **Table S7: Genes whose alterations in expression correlate to opening or closing of the chromatin**
1050
1051 **Table S8: Genes whose alterations in expression correlate to opening or closing of the chromatin in region located**
1052 **+/- 8kb around the TSS.**
1053
1054 **Table S9:** ATAC-Seq peaks associated with upregulated genes and revealing the existence of paired TFBS motifs
1055
1056 **Table S10:** Hogan (HAECS) (list of human gene names and the corresponding orthologue genes in mice, that have
1057 been used for the cross-species comparison.
1058
1059 **Table S11: List of the RT-qPCR primers**
1060
1061 **Jupyter notebook: ATAC-seq workflow**
1062 Detailed and explained bioinformatics workflow used for the analysis of ATAC-seq dataset.
1063

ACKNOWLEDGEMENTS

We are grateful to Dr. Kevin Cheeseman and Dr Magali Hennion (UMR7216) for helpful discussions and comments on the manuscript. This work benefited from equipment and services from the iGenSeq core facility, at the Institut du Cerveau et de la Moëlle (Paris, France). We are particularly grateful to Yannick Marie, the Head of iGenSeq core facility) and Emeline Mundwiller. We are grateful to Dr Sheila Harroch (Pasteur Institute, Paris, France) for the kind gift of the Oli-neu cell line. The authors acknowledge the support of the Freiburg Galaxy Team. We thank the Buffon animal housing facilities at the Jacques Monod Institute and at Robert Debré Hospital (University of Paris, Paris, France).

Figure 1

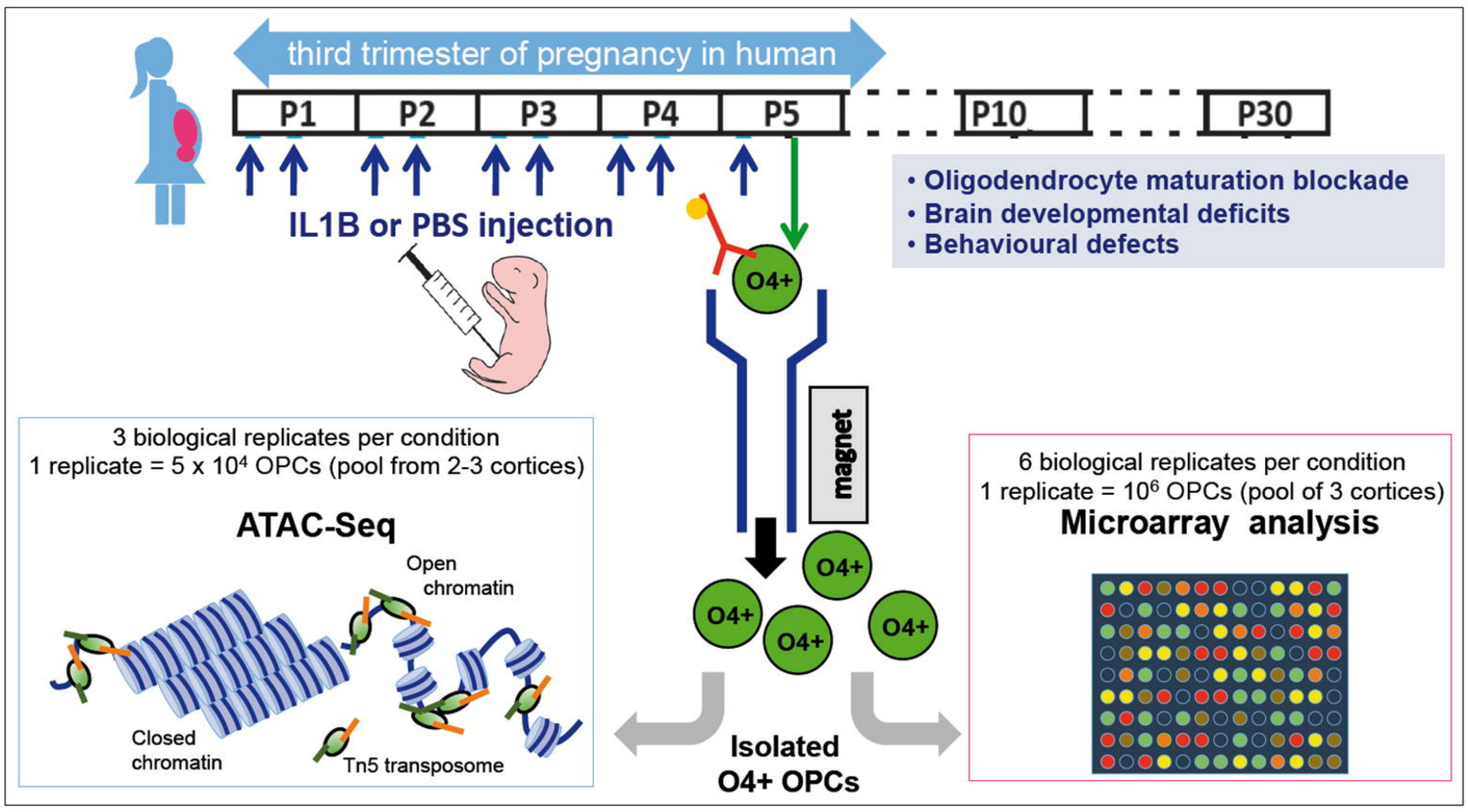
third trimester of pregnancy in human
P1
P2
P3
P4
P5
P10
P30
IL1B or PBS injection
• Oligodendrocyte maturation blockade
• Brain developmental deficits
• Behavioural defects
O4+
magnet
3 biological replicates per condition
1 replicate = 5 x 10⁴ OPCs (pool from 2-3 cortices)
ATAC-Seq
Open chromatin
Closed chromatin
Tn5 transposome
Isolated O4+ OPCs
6 biological replicates per condition
1 replicate = 10⁶ OPCs (pool of 3 cortices)
Microarray analysis

Figure 2

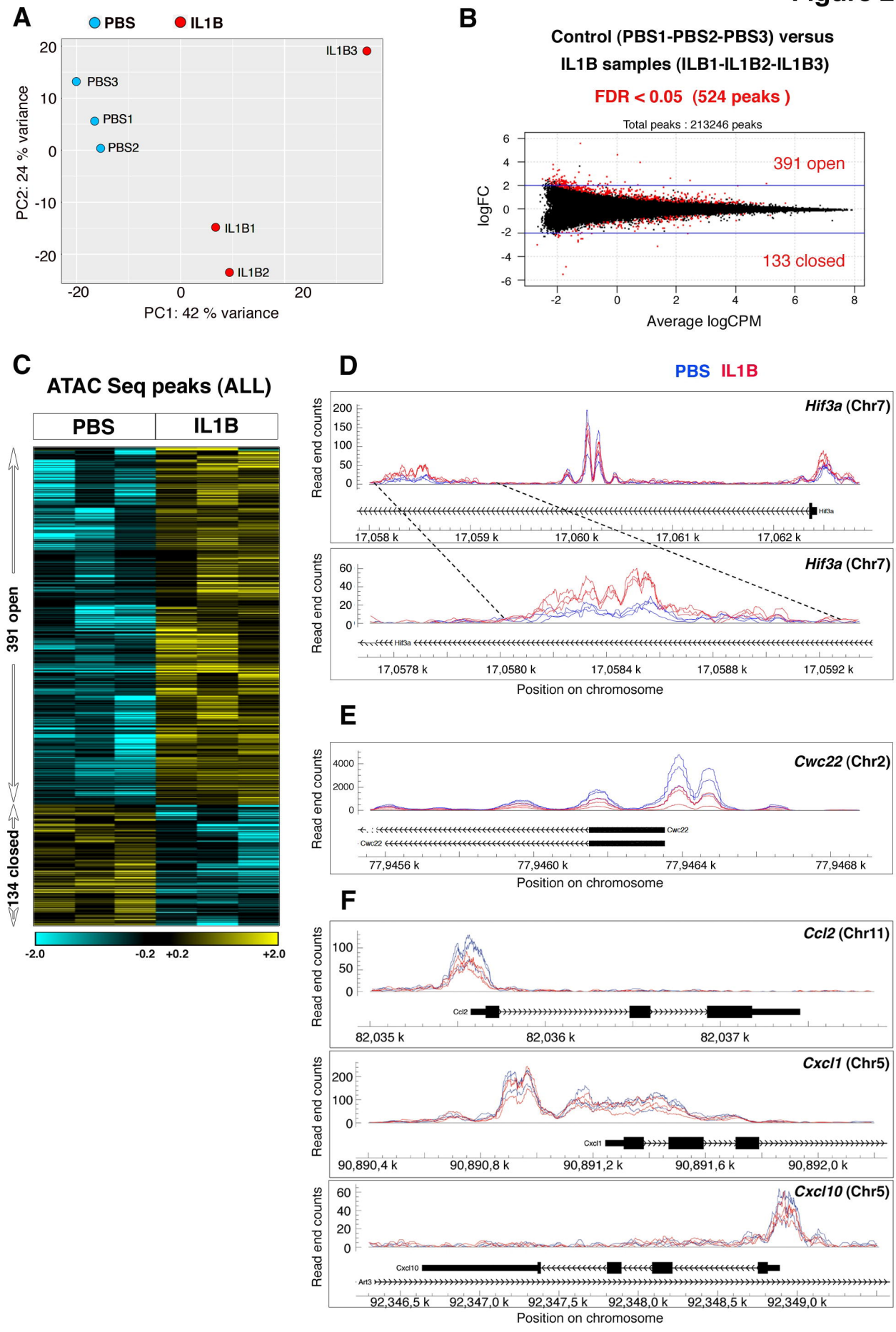
A
PBS
IL1B
IL1B3
PBS3
PBS1
PBS2
IL1B1
IL1B2
PC2: 24 % variance
PC1: 42 % variance
B
Control (PBS1-PBS2-PBS3) versus
IL1B samples (ILB1-IL1B2-IL1B3)
FDR < 0.05 (524 peaks)
Total peaks : 213246 peaks
391 open
133 closed
logFC
Average logCPM
C
ATAC Seq peaks (ALL)
PBS
IL1B
391 open
134 closed
-2.0
-0.2
+0.2
+2.0
D
PBS IL1B
Hif3a (Chr7)
Read end counts
Position on chromosome
E
Cwc22 (Chr2)
F
Ccl2 (Chr11)
Cxcl1 (Chr5)
Cxcl10 (Chr5)

Figure 3

A

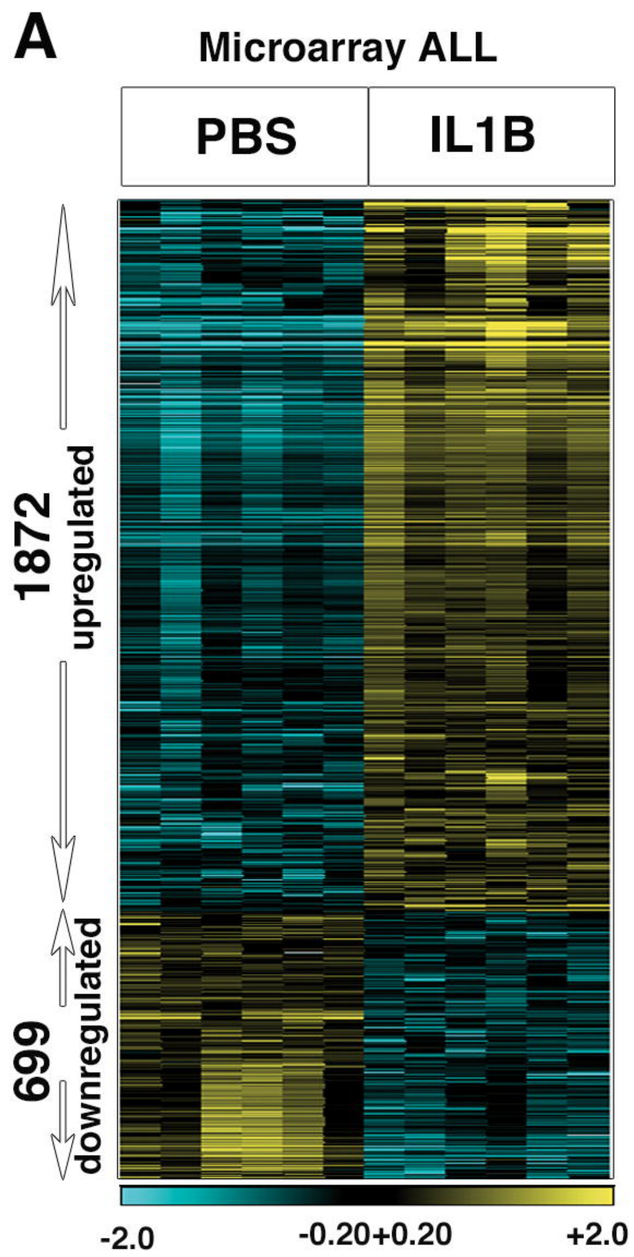

B

Category	Term	Count	PValue	Fold Enrichment	FDR
GOTERM_BP_	GO:0002376~immune system process	128	9.06E-69	6.47E+00	1.67E-65
GOTERM_BP_	GO:0006954~inflammatory response	105	8.35E-52	5.91E+00	1.54E-48
GOTERM_BP_	GO:0045087~innate immune response	102	1.89E-42	4.94E+00	3.48E-39
GOTERM_BP_	GO:0006955~immune response	69	1.64E-28	4.91E+00	3.03E-25
GOTERM_BP_	GO:0006935~chemotaxis	38	1.10E-19	6.23E+00	2.03E-16
GOTERM_BP_	GO:0051607~defense response to virus	42	2.20E-17	4.87E+00	4.06E-14
GOTERM_BP_	GO:0035458~cellular response to interferon-beta	21	1.44E-15	9.92E+00	2.66E-12
GOTERM_BP_	GO:0032496~response to lipopolysaccharide	42	1.25E-14	4.13E+00	2.31E-11
GOTERM_BP_	GO:0071222~cellular response to lipopolysaccharide	43	2.14E-14	3.98E+00	3.93E-11
GOTERM_BP_	GO:0050830~defense response to Gram-positive bacterium	28	9.00E-14	5.83E+00	1.66E-10

C

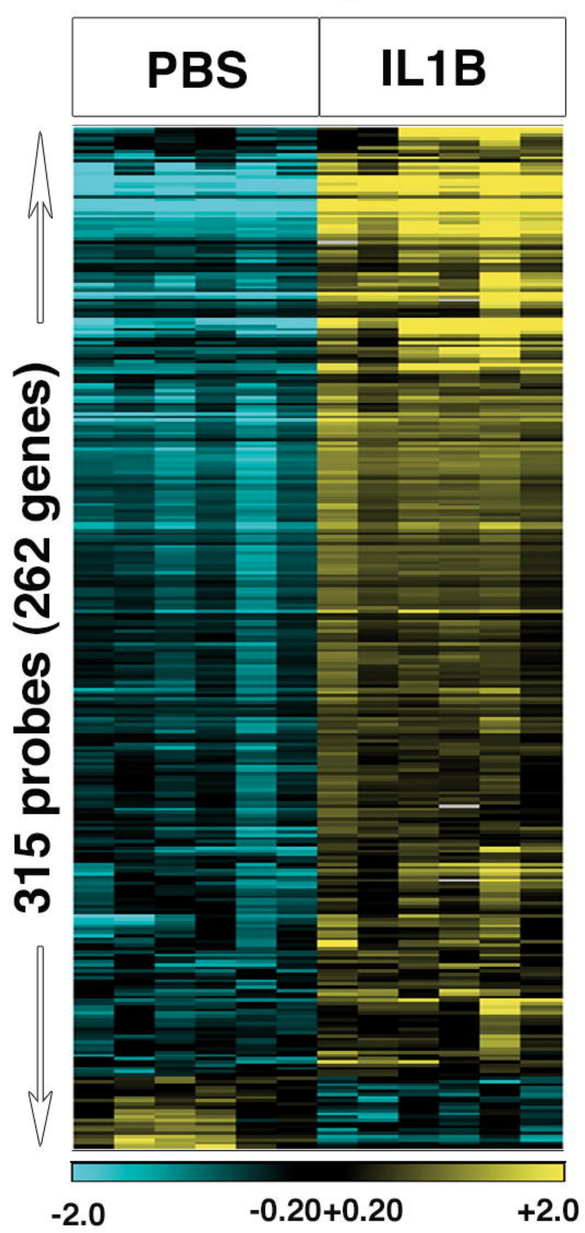

D

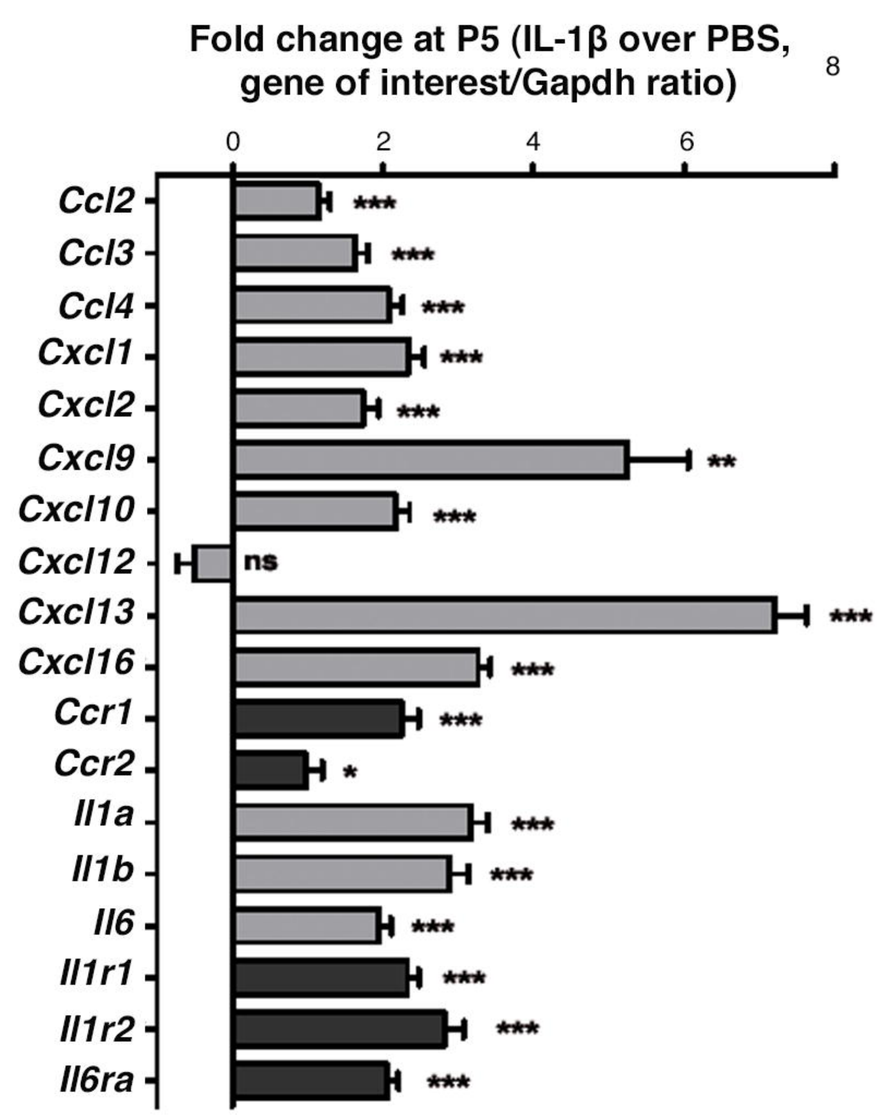

Figure 4

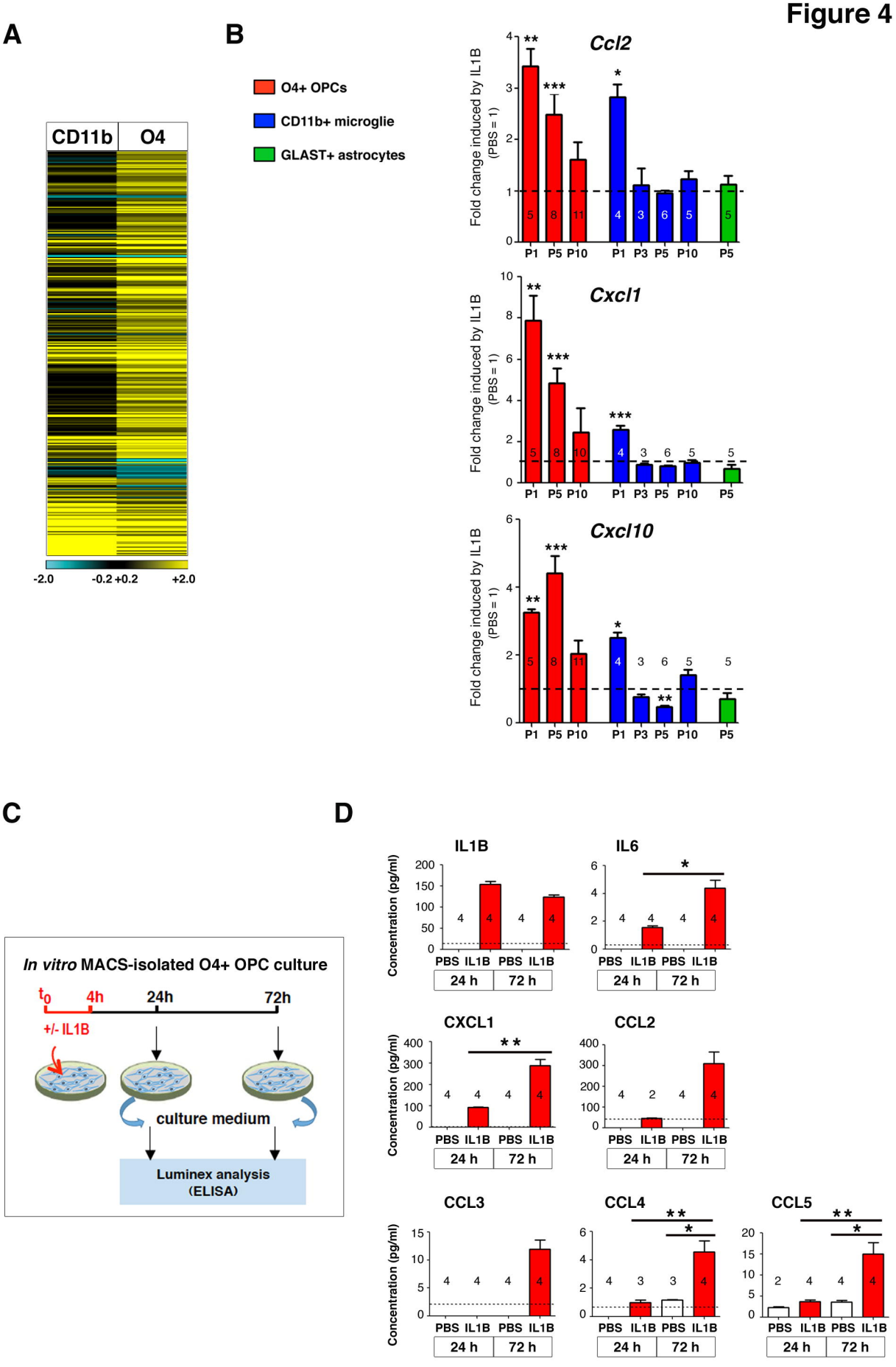
A
CD11b
O4
-2.0
-0.2 +0.2
+2.0
B
O4+ OPCs
CD11b+ microglie
GLAST+ astrocytes
Ccl2
Cxcl1
Cxcl10
Fold change induced by IL1B (PBS = 1)
P1 P5 P10 P1 P3 P5 P10 P5
C
In vitro MACS-isolated O4+ OPC culture
t0 4h 24h 72h
+/- IL1B
culture medium
Luminex analysis (ELISA)
D
IL1B
IL6
CXCL1
CCL2
CCL3
CCL4
CCL5
Concentration (pg/ml)
PBS IL1B PBS IL1B
24 h 72 h

Figure 5

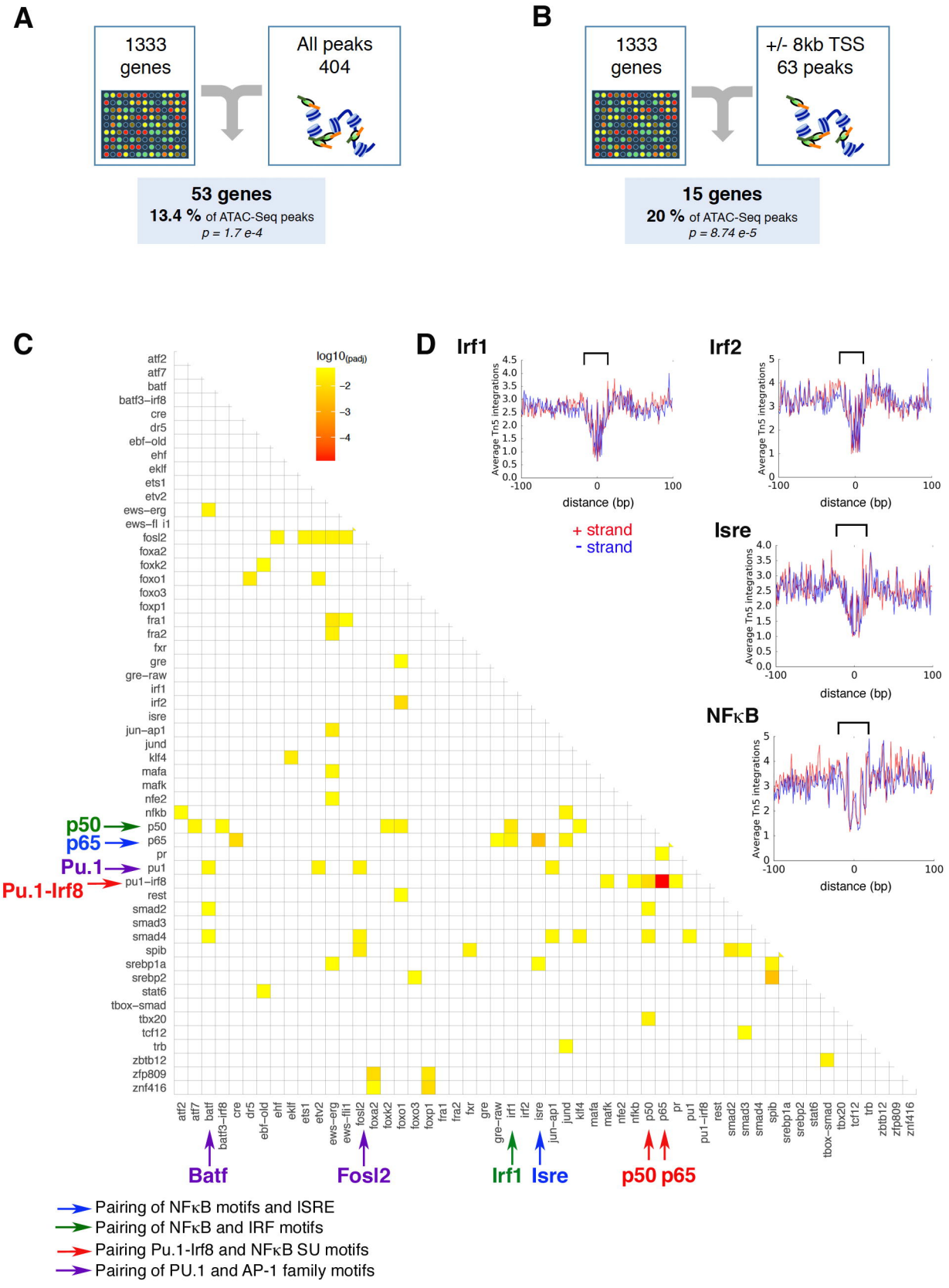
A
1333 genes
All peaks 404
53 genes
13.4 % of ATAC-Seq peaks
p = 1.7 e-4
B
1333 genes
+/- 8kb TSS 63 peaks
15 genes
20 % of ATAC-Seq peaks
p = 8.74 e-5
C
log10(padj)
p50
p65
Pu.1
Pu.1-Irf8
Batf
Fosl2
Irf1
Isre
p50 p65
D
Irf1
Irf2
Isre
NFκB
Average Tn5 integrations
distance (bp)
+ strand
- strand
Pairing of NFκB motifs and ISRE
Pairing of NFκB and IRF motifs
Pairing Pu.1-Irf8 and NFκB SU motifs
Pairing of PU.1 and AP-1 family motifs

Figure 6

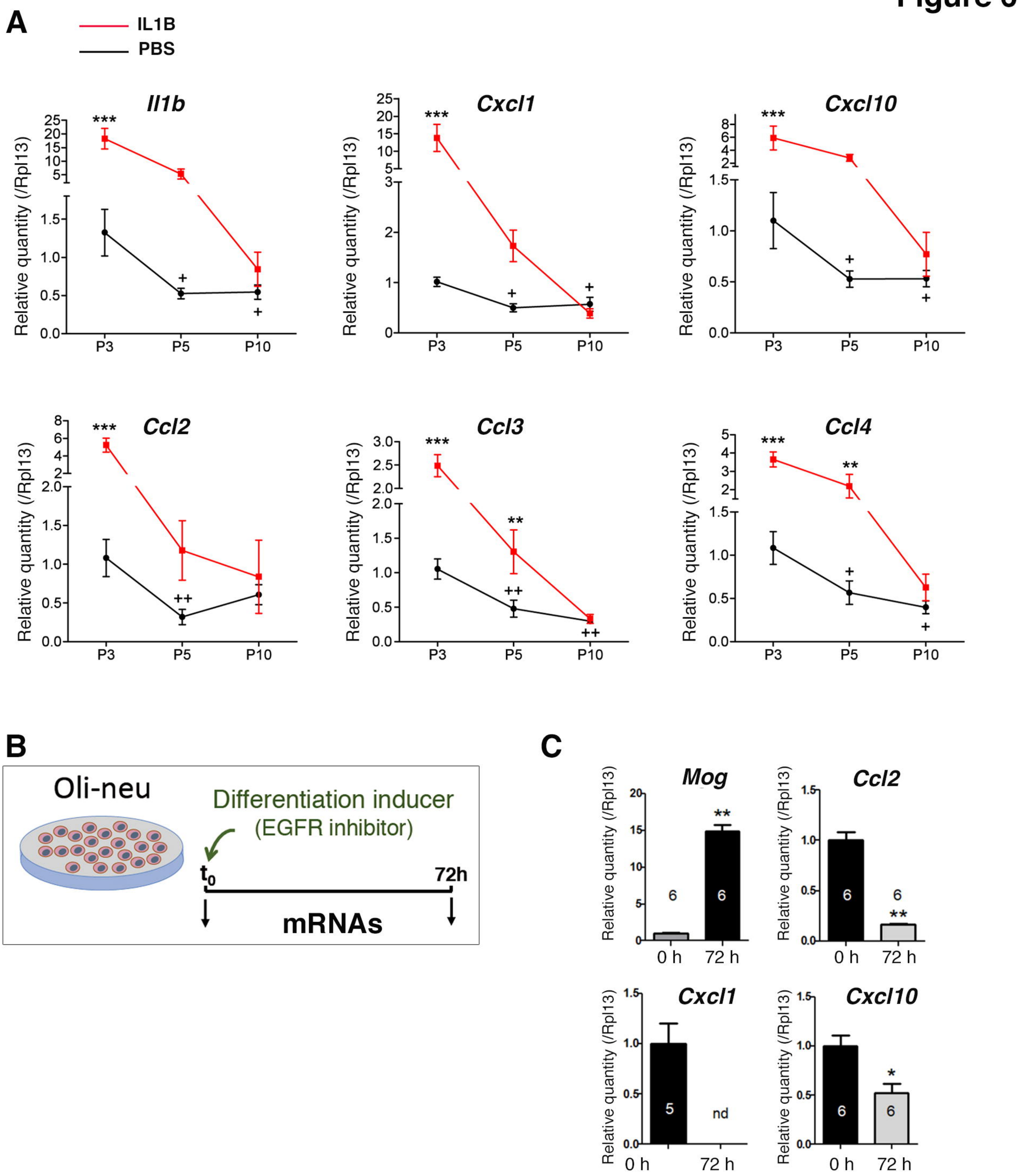
A
IL1B
PBS
Il1b
Cxcl1
Cxcl10
Ccl2
Ccl3
Ccl4
Relative quantity (/Rpl13)
P3
P5
P10
B
Oli-neu
Differentiation inducer
(EGFR inhibitor)
t0
72h
mRNAs
C
Mog
Ccl2
Cxcl1
Cxcl10
0 h
72 h
nd

Figure 7

A

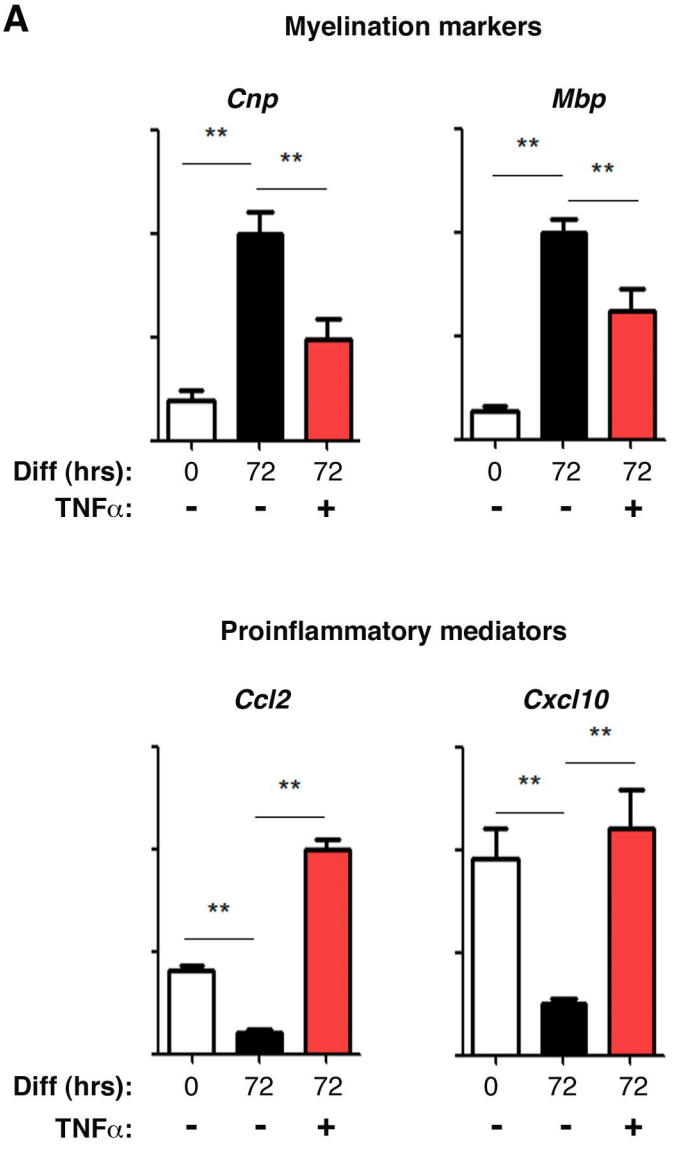
Myelination markers
Cnp
Mbp
**
**
**
**
Diff (hrs): 0 72 72 0 72 72
TNFα: - - + - - +
Proinflammatory mediators
Ccl2
Cxcl10
**
**
**
**
Diff (hrs): 0 72 72 0 72 72
TNFα: - - + - - +